THE JOURNAL OF CELL BIOLOGY

ROCK-I regulates closure of the eyelids and ventral body wall by inducing assembly of actomyosin bundles

Yoshihiko Shimizu,[1,2] Dean Thumkeo,[1] Jeongsin Keel,[1] Toshimasa Ishizaki,[1] Hiroko Oshima,[1] Masanobu Oshima,[1] Yoichi Noda,[2] Fumio Matsumura,[3] Makoto M. Taketo,[1] and Shuh Narumiya[1]

[1]Department of Pharmacology, Kyoto University Faculty of Medicine, Sakyo-ku, Kyoto 606-8501, Japan
[2]Department of Obstetrics and Gynecology, Shiga University of Medical Science, Ohtsu, Shiga 520-2191, Japan
[3]Department of Molecular Biology and Biochemistry, Rutgers University, Piscataway, NJ 08855

Rho-associated kinase (ROCK) I mediates signaling from Rho to the actin cytoskeleton. To investigate the in vivo functions of ROCK-I, we generated ROCK-I–deficient mice. Loss of ROCK-I resulted in failure of eyelid closure and closure of the ventral body wall, which gave rise to the eyes open at birth and omphalocele phenotypes in neonates. Most ROCK-I$^{-/-}$ mice died soon after birth as a result of cannibalization of the omphalocele by the mother. Actin cables that encircle the eye in the epithelial cells of the eyelid were disorganized and accumulation of filamentous actin at the umbilical ring was impaired, with loss of phosphorylation of the myosin regulatory light chain (MLC) at both sites, in ROCK-I$^{-/-}$ embryos. Stress fiber formation and MLC phosphorylation induced by EGF were also attenuated in primary keratinocytes from ROCK-I$^{-/-}$ mice. These results suggest that ROCK-I regulates closure of the eyelids and ventral body wall through organization of actomyosin bundles.

Introduction

The small GTPase Rho contributes to cellular functions such as cell motility, adhesion, and cytokinesis through reorganization of the actin cytoskeleton. Rho is activated by extracellular signals such as lysophosphatidic acid as well as during progression of the cell cycle. Rho activation results in assembly of contractile actin–myosin bundles, which include stress fibers in interphase cells and the contractile ring in dividing cells (Narumiya, 1996; Etienne-Manneville and Hall, 2002). The actions of Rho are mediated by downstream Rho effectors, a variety of which have been identified on the basis of their selective interaction with the active form of Rho. One such effector is Rho-associated kinase (ROCK), which includes ROCK-I (also known as ROK β) and ROCK-II (also known as Rho-kinase or ROK α; Riento and Ridley, 2003). ROCK mediates Rho signaling and reorganizes the actin cytoskeleton through phosphorylation of several substrates that contribute to the assembly of actin filaments and contractility. For example, ROCK phosphorylates both the myosin regulatory light chain (MLC) and myosin phosphatase, thereby regulating the level of MLC phosphorylation both directly and indirectly (Amano et al., 2000). Phosphorylation of MLC induces smooth muscle contraction as well as the formation of both stress fibers and focal adhesions. ROCK also phosphorylates and activates LIM-kinase, which in turn phosphorylates the cofilin/actin-depolymerizing factor complex and thereby inhibits its ability to mediate depolymerization and severing of actin filaments (Maekawa et al., 1999).

Elucidation of the roles of ROCK in the intact mammalian body has been facilitated by the introduction of a specific ROCK inhibitor, Y-27632 (Uehata et al., 1997). Studies with this inhibitor have revealed that ROCK regulates various physiological and pathological processes including smooth muscle contraction associated with hypertension and asthma, and cell migration associated with inflammation and tumor metastasis. However, relatively little is known of the role of ROCK in development. In addition, given that Y-27632 inhibits the activity of both ROCK-I and ROCK-II, studies with this inhibitor provide limited information on the specific functions of each ROCK isoform. To explore such specific functions of ROCK-I and ROCK-II, we have generated mice deficient in these enzymes individually. We previously described the generation and phenotype of ROCK-II knockout mice (Thumkeo et al., 2003). Most

Y. Shimizu and D. Thumkeo contributed equally to this work.

J. Keel was deceased on 6 September 2000.

Correspondence to Shuh Narumiya: snaru@mfour.med.kyoto-u.ac.jp

Abbreviations used in this paper: α-SMA, α-smooth muscle actin; dpc, d postcoitum; EGFR, EGF receptor; EOB, eyes open at birth; JNK, c-Jun NH_2-terminal kinase; MLC, myosin regulatory light chain; ROCK, Rho-associated kinase.

The Rockefeller University Press $8.00
The Journal of Cell Biology, Vol. 166, No. 6, March 14, 2005 941–953
http://www.jcb.org/cgi/doi/10.1083/jcb.200411179

ROCK-II–deficient embryos manifest extensive thrombus formation in the placenta, resulting in placental dysfunction, intrauterine growth retardation, and fetal death. These animals thus revealed an important role for ROCK-II in placental homeostasis during the perinatal period.

Closure and subsequent reopening of the eyelids are common to all mammals during development. In mice, eyelid closure occurs between 15.5 and 16.5 d postcoitum (dpc), when the outermost epithelial layer of the eyelid rim extends toward the center to cover the entire ocular surface and fuses with the opposite eyelid epithelium. The eyelids are tightly closed at birth and remain so until 12 d after birth, with complete separation occurring 1 or 2 d later (Findlater et al., 1993; Kaufman, 2002). Mutations of several genes cause the eyes open at birth (EOB) phenotype. Implication of EGF receptor (EGFR) signaling in the eyelid closure and its similarity to dorsal closure in *Drosophila* are discussed (Martin and Parkhurst, 2004; Xia and Karin, 2004).

Another example of tissue closure during mammalian development is closure of the ventral body wall. At midgestation, visceral organs rapidly expand in volume and exceed the space of the peritoneal cavity, resulting in protrusion of the midgut loop from this cavity through the umbilical ring. This "physiological umbilical hernia" is first apparent at 10.5 dpc in mice. At 15.5 dpc, the midgut loop begins to return to the peritoneal cavity, and by 16.5 dpc the physiological umbilical hernia has disappeared with closure of the umbilical ring and resorption of the space formerly occupied by the gut within the umbilical cord (Kaufman, 2002). Failure of umbilical ring closure results in omphalocele, in which organs such as the liver and gut protrude from the peritoneal cavity.

We now show that ROCK-I knockout mice exhibit both EOB and omphalocele phenotypes as a result of disorganization of actomyosin cables in the eyelid epithelium and defective actin assembly in the umbilical ring.

Results

Targeted disruption of the mouse ROCK-I gene

We disrupted the ROCK-I gene by replacing exons 3 and 4, which encode part of the kinase domain, with genes for β-galactosidase and neomycin resistance (Fig. 1 A). Chimeric mice were generated, and males were mated with C57BL/6N females to produce heterozygous ROCK-I$^{+/-}$ mice, which were then intercrossed. The genotypes of offspring were determined by Southern blot analysis and PCR with DNA obtained from the tail (Fig. 1, B and C). Loss of ROCK-I protein was confirmed by immunoblot analysis (Fig. 1 D). A 160-kD protein corresponding to ROCK-I was detected in the adult brain of wild-type mice but not in that of ROCK-I$^{-/-}$ mice. In contrast, the abundance of ROCK-II did not differ between the two genotypes, indicating that the expression of ROCK-II did not increase to compensate for the loss of ROCK-I. We made use of the *lacZ* reporter gene inserted in-frame with the initiator methionine codon of ROCK-I in the targeting construct to examine the pattern of ROCK-I gene expression by whole-mount staining of ROCK-I$^{-/-}$ embryos for β-galactosidase activity with the substrate X-Gal. Such staining was detected in many locations throughout the embryo, including the skin, heart, aorta, umbilical blood vessels, and dorsal root ganglia (Fig. 1 E).

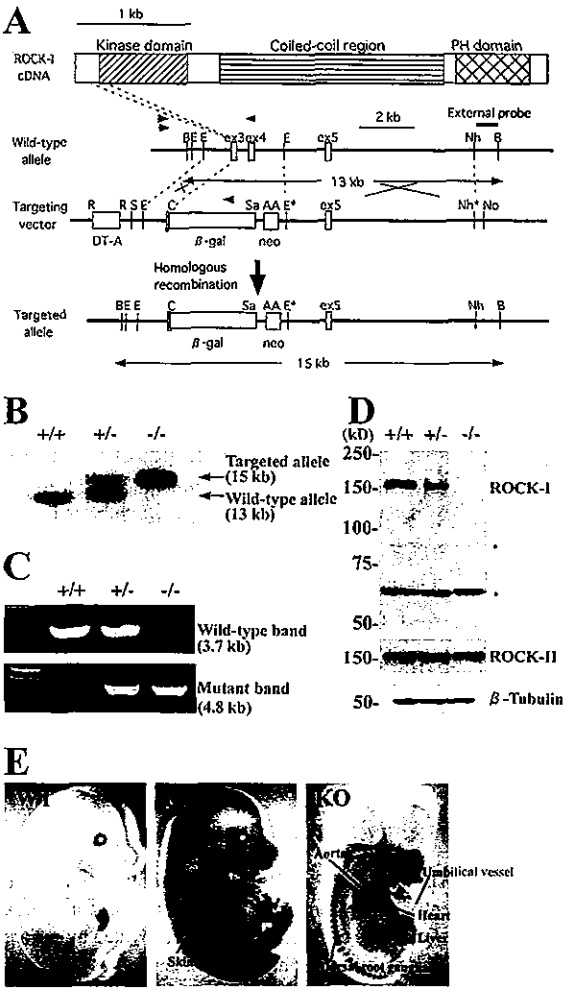

Figure 1. **Generation of ROCK-I–deficient mice.** (A) Schematic representations of the domain structure of mouse ROCK-I cDNA, the wild-type ROCK-I allele, the targeting vector, and the targeted allele. Positions of β-galactosidase (β-gal), neomycin resistance (neo), and diphtheria toxin A (DT-A) genes; of restriction sites for BglII (B), EcoRV (E), NheI (Nh), RsrII (R), SmaI (S), ClaI (C), SalI (Sa), AscI (A), and NotI (No); and of exons 3 (ex3), 4, and 5 are shown. The restriction sites indicated by asterisks are lost due to blunt-end ligation. Positions of primers for PCR analysis are indicated by arrowheads. The external probe is a unique 3′ genomic probe that distinguishes the 13-kb wild-type BglII fragment from the 15-kb BglII fragment generated by the targeted allele. (B) Southern blot analysis of genomic DNA obtained from mouse tail. The genotypes of the wild-type, heterozygous, and homozygous knockout mice are shown as +/+, +/−, and −/−, respectively. (C) Genotyping by PCR analysis of genomic DNA from mouse tail. The leftmost lane contains molecular size standards. (D) Immunoblot analysis of whole-brain lysates of adult ROCK-I$^{+/+}$, ROCK-I$^{+/-}$, and ROCK-I$^{-/-}$ mice with antibodies specific for either ROCK-I, ROCK-II, or β-tubulin. Positions of molecular mass markers are shown on the left. Asterisks indicate nonspecific bands. (E) X-Gal staining of wild-type (WT) and ROCK-I$^{-/-}$ (KO) embryos at 15.5 dpc (left and middle) or 13.5 dpc (right, sagittal section). X-Gal staining was detected in the skin, heart, aorta, umbilical blood vessels, and dorsal root ganglia of ROCK-I$^{-/-}$ embryos.

Table I. **Genotypes of offspring obtained by crossing of ROCK-I$^{+/-}$ mice**

Stage	Total no. of offspring	No. of mice of each genotype		
		+/+	+/−	−/−
14.5 dpc	40	12	20	8
15.5 dpc	145	40	73	32
16.5 dpc	56	14	28	14
18.5 dpc	344	86	168	90
4 wk	316	101	203	12

EOB and omphalocele phenotypes of ROCK-I-deficient mice

Analysis of genotype distribution in offspring from heterozygote crosses revealed that the homozygous mutant mice were present in the expected Mendelian ratio during embryonic development at all stages including 18.5 dpc. However, the ROCK-I$^{-/-}$ mice were greatly underrepresented among littermates at 4 wk old (Table I).

Examination of embryos at 18.5 dpc revealed EOB and omphalocele phenotypes that were fully penetrant in ROCK-I$^{-/-}$ mice (Fig. 2 A). At this stage of development, wild-type mice manifest fused eyelids and resolution of the physiological umbilical hernia. There was no substantial difference between wild-type and ROCK-I$^{+/-}$ littermates in this regard (unpublished data). Different degrees of fusion impairment were apparent in the eyelids of ROCK-I$^{-/-}$ mice; 50% (17/34) of such embryos had fully open eyelids, whereas the eyelids of the remaining 50% (17/34) of embryos were almost fully fused but manifested a hole with a diameter of <1 mm (Fig. 2 B). Some of the surviving ROCK-I$^{-/-}$ mice gradually developed apparent proliferative inflammation of the eyelid that almost covered the entire eye; this phenotype was observed in 50% (6/12) of ROCK-I$^{-/-}$ mice at 5–6 mo old (Fig. 2 C). This eye lesion may result from secondary effects due to the open state of the eye in neonates.

Omphalocele was apparent also in varying degrees and was classified into three types (Fig. 2 A): severe omphalocele, including the liver and small intestine (9/34, 26.5%); moderate omphalocele, with only the small intestine protruding (13/34, 38.2%); and mild omphalocele, in which the intestine protrudes upon crying (12/34, 35.3%). There was no correlation between the extent of EOB and that of omphalocele. The presence of an omphalocele does not affect survival in utero, and we found that the loss of ROCK-I$^{-/-}$ mice occurred immediately after birth. The umbilicus was not closed and intraperitoneal bleeding was evident in the dead ROCK-I$^{-/-}$ neonates (Fig. 2 D). We further noted that parts of several visceral organs, notably the liver and intestine, had been gnawed at in mutant neonates (Fig. 2, E and F). Because we confirmed that visceral organs were fully intact in 18.5 dpc mutant (not depicted), these results indicate that the mother had cannibalized the omphalocele together with the protruded organs in the process of clearing

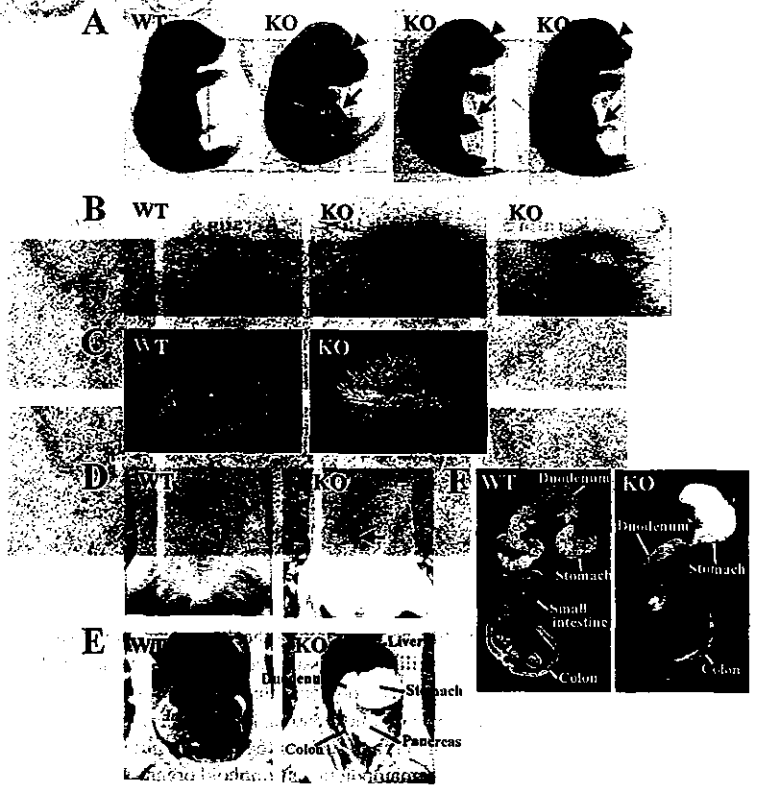

Figure 2. **EOB and omphalocele phenotypes of ROCK-I–deficient mice.** (A) Wild-type and ROCK-I$^{-/-}$ embryos at 18.5 dpc. Arrowheads and arrows indicate EOB and omphalocele phenotypes, respectively. Severe, moderate, and mild forms of omphalocele in the mutant embryos are shown from left to right. (B) Eyes of wild-type and ROCK-I$^{-/-}$ mice at 18.5 dpc. The eyes of the ROCK-I$^{-/-}$ embryos are either fully open (middle) or partially open (right; arrow indicates a small hole). (C) Eyes of adult wild-type and ROCK-I$^{-/-}$ mice. (D) Umbilical region of wild-type and ROCK-I$^{-/-}$ neonates. The umbilical ring in the wild-type neonate is closed (arrowhead), whereas that in the ROCK-I$^{-/-}$ neonate remains open (arrow). (E) Visceral organs in the abdominal cavity of the neonates shown in D. The ventral body wall was removed to render the visceral organs visible. Portions of the liver and intestine are absent in the ROCK-I$^{-/-}$ neonate. (F) Gastrointestinal tract from the stomach to the colon of the neonates shown in D and E. A part of the small intestine is absent in the ROCK-I$^{-/-}$ mouse.

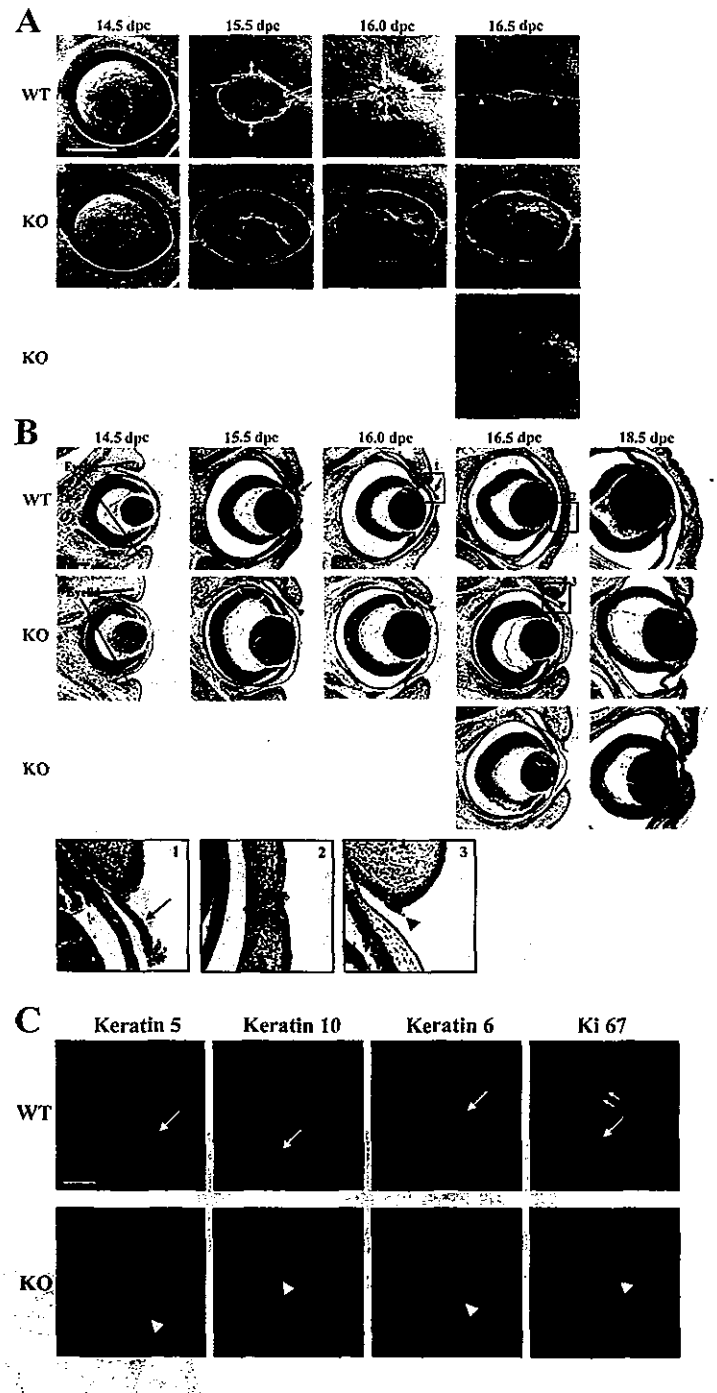

Figure 3. **Impaired eyelid closure in ROCK-I$^{-/-}$ embryos.** (A) Scanning electron micrographs of the eyes of wild-type (top) and ROCK-I$^{-/-}$ (middle and bottom) embryos from 14.5 to 16.5 dpc. Bidirectional arrows indicate extension of the eyelid rim. Arrowheads indicate eyelid fusion in the wild-type embryos. Bar, 500 μm. (B) Hematoxylin-eosin staining of transverse eye sections from wild-type and ROCK-I$^{-/-}$ embryos from 14.5 to 18.5 dpc. Arrows indicate the eyelid epithelial sheet extending from the rim of the eyelid in the wild-type embryos. Eyelid epithelial extension was impaired in mutant embryos, with arrowheads indicating the cell mass at the expected site of sheet formation. Bar, 200 μm. Boxed regions 1–3 are also shown enlarged. Bar, 20 μm. (C) Immunofluorescence staining (green) for keratins 5, 10, and 6 as well as for Ki67 in frozen sections of the eyelids of wild-type or ROCK-I$^{-/-}$ embryos at 16.0 dpc. Nuclei are stained blue. Large arrows indicate the eyelid epithelial sheet; arrowheads indicate the epithelial cell mass. The two small arrows indicate the base of the eyelid epithelial sheet. Bar, 50 μm.

the placenta and umbilicus, causing the death of these neonates. Most ROCK-I$^{-/-}$ neonates therefore do not survive, leaving only a small proportion to grow to adulthood.

Most of the surviving ROCK-I$^{-/-}$ mice, both male and female, subsequently developed normally, with the exception of the eye lesions described above, and the adult mutant animals were fertile and apparently healthy. Two adult ROCK-I$^{-/-}$ mice were killed and tissue sections were stained with hematoxylin-eosin. No obvious abnormality was observed in the brain, spinal cord, heart, aorta, lung, trachea, kidney, or bladder; in endocrine organs such as the thyroid, pituitary, and adrenal glands; in hematopoietic or lymphoid organs such as bone mar-

row, spleen, thymus, and lymph nodes; in the gastrointestinal tract from the tongue to the rectum; in reproductive organs including testis, epididymis, seminal vesicle, prostate gland, ovary, and uterus; or in the epidermis and dermis of the skin (unpublished data). In addition, no marked difference in systolic blood pressure, as measured by a noninvasive tail-cuff method, was found between wild-type and ROCK-I$^{-/-}$ mice (138 ± 10 and 134 ± 6 mmHg, respectively, $n = 5$).

Impaired extension of the eyelid epithelial sheet in ROCK-I$^{-/-}$ embryos

To elucidate the molecular mechanism responsible for the failure of eyelid closure in ROCK-I$^{-/-}$ embryos, we first examined wild-type and homozygous mutant embryos at various stages by scanning electron microscopy (Fig. 3 A). Typically, at 14.5 dpc, wild-type and ROCK-I$^{-/-}$ embryos manifested open eyes of similar shape and with no distinct morphological difference. Differences between the genotypes were evident at 15.5 and 16.0 dpc, however. In wild-type embryos, the rims of the top and bottom eyelids extended toward each other and fused from both nasal and lateral margins. In contrast, the eyelids of many ROCK-I$^{-/-}$ embryos failed to extend during this period, leaving the ocular surface exposed. Whereas the eyelids of wild-type embryos were completely fused at the midline by 16.5 dpc, two different degrees of failure of eyelid closure (fully open eyes or partially fused eyelids) were apparent in the eyes of ROCK-I$^{-/-}$ mice at this time.

We next compared eyelid closure in wild-type and ROCK-I$^{-/-}$ embryos by histological analysis (Fig. 3 B). Similar to the skin in other regions of the body, the eyelid consists of epithelium and dermis. In wild-type embryos, the eyelid epithelium comprises a single layer of basal cells at 14.5 dpc and becomes multilayered as a result of proliferation and differentiation of the basal cells between 15.5 and 16.0 dpc. Around this time, the eyelid epithelial sheet extends from both top and bottom eyelid tips to cover the ocular surface. The two sheets meet at the center and eventually fuse each other at 16.5 dpc. The eyelid morphology of ROCK-I$^{-/-}$ embryos appeared identical to that of their wild-type littermates at 14.5 dpc. The eyelid epithelium also became multilayered in the mutant mice between 15.5 and 16.0 dpc. However, the ROCK-I$^{-/-}$ embryos failed to extend the eyelid epithelial sheet. At 16.5 dpc, the ROCK-I$^{-/-}$ embryos had only partially extended the eyelid epithelial sheets or had not done so at all. Consequently, the eye of ROCK-I$^{-/-}$ embryos was open by varying degrees at 18.5 dpc. These results suggest that the EOB phenotype of ROCK-I$^{-/-}$ mice is caused by impaired or delayed extension of the eyelid epithelial sheet.

To characterize the cells present in the eyelid epithelial sheet, we performed immunofluorescence staining for keratins 5, 10, and 6, which are markers of epithelial cell differentiation (Fig. 3 C; Fuchs, 1996; Mazzalupo and Coulombe, 2001). The eyelid epithelial sheet of wild-type embryos was positive for keratin 5 and negative for keratin 10, indicative of its basal cell composition. The sheet was also positive for keratin 6. A similar staining pattern was apparent for the cell mass at the expected site of sheet formation in ROCK-I$^{-/-}$ mice. In addition, the base of the eyelid epithelial sheet in wild-type embryos and that of the cell mass in ROCK-I$^{-/-}$ embryos were rich in cells positive for Ki67, a marker of cell proliferation. These results indicate the presence of a population of normally differentiated cells in the eyelid of ROCK-I$^{-/-}$ mice.

Impaired formation of actomyosin cables in the eyelid epithelial cells of ROCK-I$^{-/-}$ embryos

Given that ROCK induces myosin-mediated cross-linking of actin filaments and consequently makes actin bundles such as stress fibers in cultured cells, we investigated whether loss of ROCK-I might impair formation of the actin architecture required for extension of the eyelid epithelial sheet and thereby cause the EOB phenotype. Whole-mount phalloidin staining of the eyelids of wild-type embryos at 15.5 and 16.0 dpc revealed the presence of thick actin cables that coursed continuously from cell to cell at the leading edge of the eyelid epithelial sheet and encompassed the circumference of the eye like a ring (Fig. 4, A–D). Pronounced phalloidin staining was also apparent in individual cells of the eyelid around the eye circumference in ROCK-I$^{-/-}$ embryos, but most of these actin filaments were not organized into cables that extended beyond each cell (Fig. 4, A and E–G). Phalloidin staining of transverse frozen sections from wild-type mice revealed that the actin cables were localized in a few layers of cells in the eyelid epithelial sheet (Fig. 4 H); they were first apparent in the eyelid tips at 15.5 dpc and had increased in number by 16.0 dpc. In contrast, the assembly of such structures was minimal in most ROCK-I$^{-/-}$ embryos at 15.5 or 16.0 dpc, although a few actin bundles were detected in some of the mutant embryos at 16.0 dpc (Fig. 4 H).

Given that ROCK regulates the phosphorylation of MLC both directly and indirectly in vitro (Amano et al., 2000), we next examined MLC phosphorylation in the eyelid epithelial sheet by staining sections of the eyelid at 16.0 dpc with antibodies specific for phosphorylated MLC (Matsumura et al., 1998). Myosin itself was uniformly stained throughout the eyelid epithelium with no difference between wild-type and ROCK-I$^{-/-}$ embryos (unpublished data). However, whereas staining for phosphorylated MLC was pronounced and associated with actin cables in the eyelid epithelial sheet of wild-type embryos, it was markedly reduced in ROCK-I$^{-/-}$ embryos (Fig. 4 I). We also prepared rabbit polyclonal antibodies to mouse ROCK-I in order to examine ROCK-I distribution during eyelid closure. Immunofluorescence staining with these antibodies revealed the presence of ROCK-I in the eyelid epithelial sheet and skin of wild-type embryos but not in ROCK-I$^{-/-}$ embryos (Fig. 4 J). A prominent ROCK-I signal was apparent in the eyelid epithelial sheet. However, staining was not specifically increased in the cells containing the actomyosin cables but rather was ubiquitous in the eyelid epithelial cells. These results suggest that local ROCK-I activation, rather than the expression level of ROCK-I, regulates the assembly of actomyosin cables during eyelid closure. Together, these observations indicate that phosphorylation of MLC occurs in a ROCK-I–dependent manner in the eyelid epithelial sheet and that this phosphorylation is required for extension of the eyelid epithelial sheet and eyelid closure.

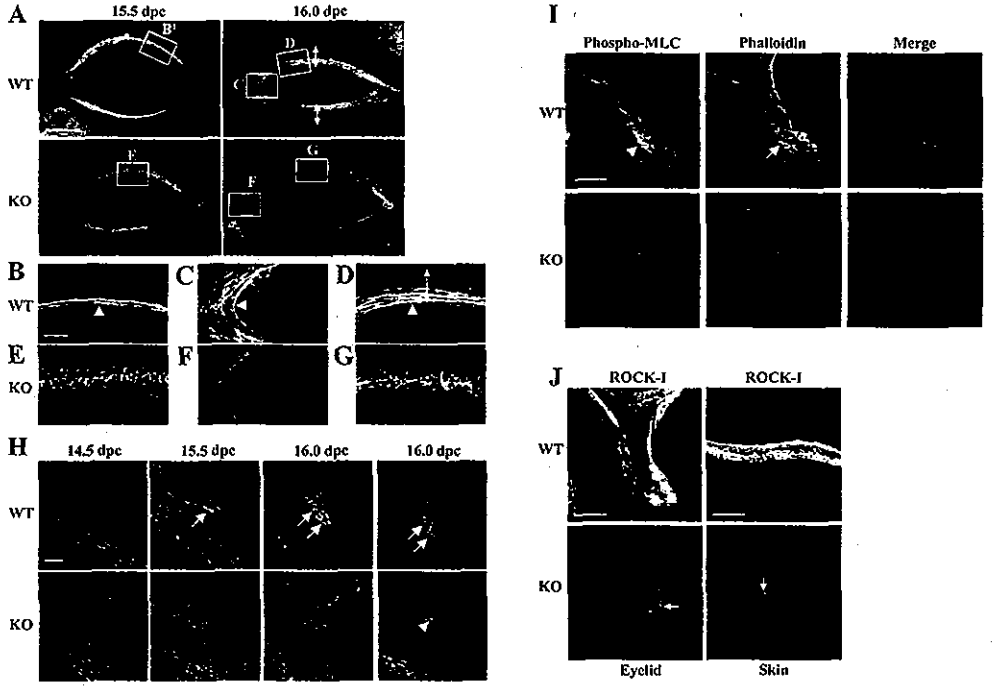

Figure 4. **ROCK-I–dependent formation of actomyosin cables in the eyelid epithelial sheet.** (A) Whole-mount phalloidin staining of the eyelids of wild-type (top) and ROCK-I$^{-/-}$ (bottom) embryos at 15.5 and 16.0 dpc. Bidirectional arrows indicate extension of the eyelid epithelial sheet. Bar, 500 μm. (B–G) Higher magnification views of the boxed regions in A. Arrowheads indicate actin cables in the eyelid epithelial sheet of wild-type embryos. Bidirectional arrows indicate extension of the eyelid epithelial sheet. ROCK-I$^{-/-}$ embryos failed to assemble continuous actin cables. Bar, 50 μm. (H) Phalloidin staining of transverse sections of the eyelid rim of wild-type (top) and ROCK-I$^{-/-}$ (bottom) embryos from 14.5 to 16.0 dpc. A substantial number of actin cables was apparent in a few layers of the eyelid epithelial sheet of wild-type embryos (arrows). Little filamentous-actin accumulation was detected in mutant embryos, with the exception of a few actin bundles in some embryos (arrowhead). Bar, 50 μm. (I) Immunofluorescence staining for phosphorylated MLC (green) and phalloidin staining (red) in sections of the eyelid of wild-type (top) and ROCK-I$^{-/-}$ (bottom) embryos at 16.0 dpc. Phosphorylated MLC was enriched in the eyelid epithelial sheet of wild-type embryos (arrowhead), where it was colocalized with actin cables (arrow). Little phosphorylated MLC staining was detected in ROCK-I$^{-/-}$ embryos. Bar, 50 μm. (J) Immunofluorescence staining for ROCK-I in sections of the eyelid (left) and skin (right) of wild-type (top) and ROCK-I$^{-/-}$ (bottom) embryos at 16.0 dpc. Nonspecific signals are indicated by arrows. Bars, 50 μm.

ROCK-I mediates MLC phosphorylation induced by EGF in primary keratinocytes

Studies with several lines of mutant mice have implicated EGF signaling in eyelid closure (Miettinen et al., 1995; Sibilia and Wagner, 1995; Threadgill et al., 1995). Therefore, we next examined the role of ROCK-I in EGF signaling in primary keratinocytes. Primary keratinocytes were isolated from wild-type and ROCK-I$^{-/-}$ embryos at 18.5 dpc and their identity was confirmed by staining for keratin 5; the presence or absence of ROCK-I, respectively, was also confirmed by immunoblot and immunofluorescence analyses (unpublished data). Measurement of the incorporation of BrdU revealed that the proliferation capacity of the ROCK-I$^{-/-}$ keratinocytes did not differ from that of the wild-type cells (Fig. 5 A), consistent with our Ki67 immunostaining data (Fig. 3 C).

Phalloidin staining showed the presence of actin filaments around the circumference of serum-deprived wild-type keratinocytes (Fig. 5 B); a few short actin bundles were also detected inside the cells. Serum-deprived ROCK-I$^{-/-}$ keratinocytes also contained circumferential actin filaments and short actin bundles. Stimulation of wild-type cells with EGF (10 ng/ml) resulted in the formation of thick actin bundles that resembled stress fibers and spanned the cell length. These actin bundles were observed in 33 and 56.4% of wild-type cells at 30 and 120 min, respectively (Fig. 5, B and C). Similar structures were also induced by EGF in ROCK-I$^{-/-}$ cells, but they were thinner and fewer in number. In addition, only 11 and 20% of ROCK-I$^{-/-}$ cells contained the actin bundles at 30 and 120 min, respectively. These results suggest that ROCK-I plays an important role in the EGF-induced formation of stress fibers in keratinocytes. The EGF-induced formation of actin bundles in both wild-type and ROCK-I$^{-/-}$ cells was prevented by the ROCK inhibitor Y-27632 (Fig. 5 B), suggesting that ROCK-II also contributes to this process.

Given that ROCK acts downstream of Rho, we next examined the possible effect of EGF stimulation on Rho activity in primary keratinocytes with the use of a pull-down assay for the GTP-bound (active) form of Rho. EGF induced a small but reproducible increase in the amount of the GTP-bound form of Rho in both wild-type and ROCK-I$^{-/-}$ keratinocytes (Fig. 5 D). Together, these results thus indicate that the Rho–ROCK signaling pathway is activated by EGF in primary keratinocytes. To elucidate the signaling events downstream of ROCK-I in

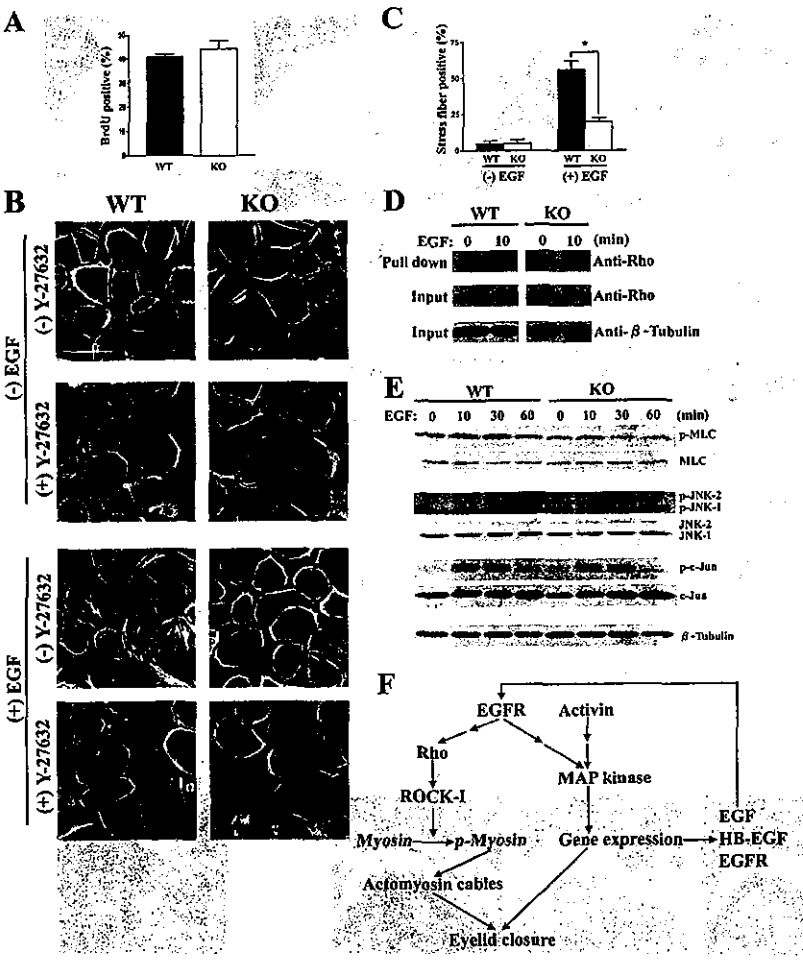

Figure 5. ***Impairment of EGF-induced formation of actin stress fibers in primary keratinocytes derived from ROCK-I$^{-/-}$ embryos.*** (A) Cell proliferation. Primary keratinocytes derived from wild-type or ROCK-I$^{-/-}$ embryos were cultured in the presence of EGF (10 ng/ml) and evaluated for cell proliferation by measurement of incorporation of BrdU. Data are expressed as the percentage of cells that were BrdU positive and are means ± SEM of values from five independent experiments. (B) Phalloidin staining of keratinocytes. Wild-type and ROCK-I$^{-/-}$ keratinocytes were maintained in serum-free medium for 24 h, cultured with or without EGF (10 ng/ml) for 2 h in the absence or presence of 10 μM Y-27632, and then subjected to staining with phalloidin. Bar, 50 μm. (C) Quantitative analysis of EGF-induced stress fiber formation. Cells incubated with or without EGF for 2 h and stained with phalloidin as in B were analyzed for determination of the percentage of cells with stress fibers. A total of 100 cells were examined for each condition. Data are means ± SEM of values from five independent experiments. *, $P < 0.05$. (D) EGF-induced Rho activation. Wild-type and ROCK-I$^{-/-}$ keratinocytes were cultured in serum-free medium for 24 h, stimulated with EGF (10 ng/ml) for 0 or 10 min, and then subjected to a pull-down assay for the GTP-bound (active) form of Rho. Rho-GTP precipitated from cell lysates was detected by immunoblot analysis with antibodies to Rho (top), and cell lysates (input) were similarly analyzed for the total amounts of Rho (middle) and β-tubulin (bottom). (E) EGF-induced MLC, JNK, and c-Jun phosphorylation. Wild-type and ROCK-I$^{-/-}$ keratinocytes were maintained in serum-free medium for 24 h before stimulation with EGF (10 ng/ml) for the indicated times. Cell lysates were then subjected to immunoblot analysis with antibodies to MLC, to phosphorylated (p-) MLC, to JNK, to phosphorylated JNK, to c-Jun, to phosphorylated c-Jun, and to β-tubulin (control). (F) Proposed role for ROCK-I in mouse eyelid closure. A Rho–ROCK-I–myosin cascade triggered by activation of the EGFR is required for the assembly of the purse stringlike actin cables that contribute to extension of the eyelid epithelial sheet. An autocrine–paracrine pathway mediated by EGFR or activin results in activation of a MAPK cascade and consequent transcription of EGF, heparin-binding EGF (HB-EGF), and EGFR genes.

EGF signaling in these cells, we examined MLC phosphorylation and the activation of c-Jun NH_2-terminal kinase (JNK) and c-Jun. The basal level of MLC phosphorylation did not differ between wild-type and ROCK-I$^{-/-}$ keratinocytes (Fig. 5 E). EGF induced a rapid and transient increase in the extent of MLC phosphorylation in wild-type keratinocytes; this effect was detectable at 10 and 30 min but no longer at 60 min. EGF-induced phosphorylation of MLC was also apparent in ROCK-I$^{-/-}$ keratinocytes at 10 min, but its extent was markedly reduced compared with that observed in wild-type cells. Moreover, MLC phosphorylation in the mutant cells had returned to the basal level by 30 min. In contrast, EGF induced the phosphorylation of JNK, as well as that of its substrate c-Jun, to similar extents in wild-type and ROCK-I$^{-/-}$ keratinocytes (Fig. 5 E). This latter finding was supported by immunofluorescence staining that revealed similar levels of c-Jun and phosphorylated c-Jun in the eyelid epithelial cells of both wild-type and ROCK-I$^{-/-}$ littermates at 16.0 dpc (unpublished data).

Impaired umbilical ring closure in ROCK-I$^{-/-}$ mice

The other major phenotype of ROCK-I$^{-/-}$ mice was omphalocele, herniation of the gut and liver through the umbilical ring in neonates (Fig. 6 A). The umbilical ring was open in wild-type embryos at 15.5 dpc, and the midgut loop protruded through the umbilical ring from the abdominal cavity (Fig. 6 B). The sac of this physiological hernia consisted of an internal lining of peritoneum and an external covering of amnion. ROCK-I$^{-/-}$ mice also showed the physiological umbilical hernia at this stage. By 16.5 dpc, the umbilical ring had closed and the gut had returned to the abdominal cavity in wild-type embryos. In contrast, the umbilical hernia persisted in ROCK-I$^{-/-}$ embryos at this time, resulting in varying degrees of omphalocele in neonates. A ridge-like structure that appeared to constrict the ventral abdominal wall at the site of entry of the umbilical cord was evident in wild-type embryos but not in ROCK-I$^{-/-}$ embryos (Fig. 6 A). Histological analysis revealed that this ridge consisted of

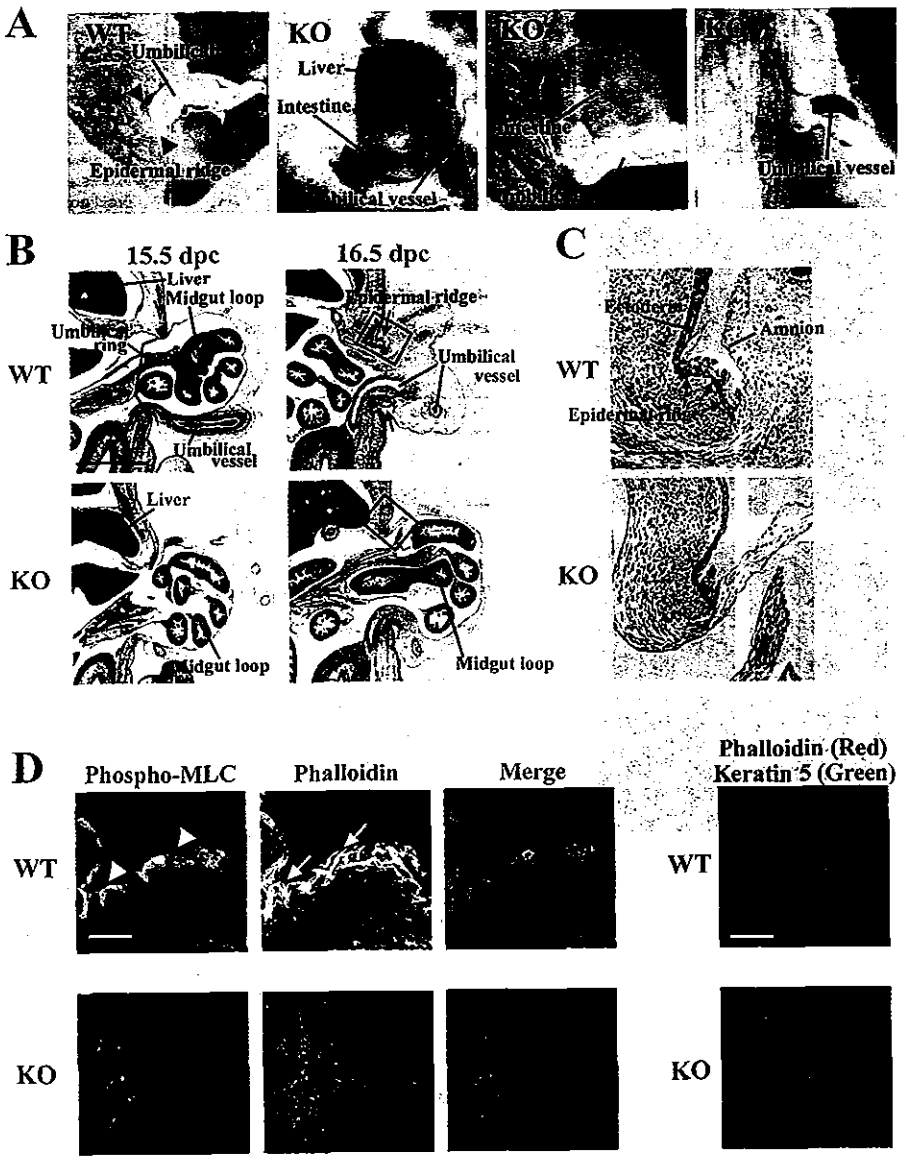

Figure 6. **Impaired closure of the umbilical ring in ROCK-I$^{-/-}$ mice.** (A) Omphalocele in ROCK-I$^{-/-}$ embryos. Wild-type and ROCK-I$^{-/-}$ embryos at 18.5 dpc are shown. Severe, moderate, and mild forms of omphalocele are apparent in the mutant mice shown in the center left, center right, and right panels, respectively. Arrowheads indicate the epidermal ridge in the wild-type embryo. (B) Hematoxylin-eosin staining of sagittal sections through the umbilical region of wild-type (top) and ROCK-I$^{-/-}$ (bottom) embryos at 15.5 (left) and 16.5 (right) dpc. Boxes indicate the region of the ectodermal–amnion transition. Arrows indicate the epidermal ridge. Bar, 1 mm. (C) Higher magnification images of the boxed regions in B. Arrows indicate the epidermal ridge in the wild-type embryo. Bar, 200 μm. (D) Staining of the epidermal ridge. Sections of the epidermal ridge of wild-type (top) and ROCK-I$^{-/-}$ (bottom) embryos at 16.5 dpc were stained with an antibody to phosphorylated MLC (green, arrowheads) and phalloidin (red, arrows) in the left panels, and with phalloidin (red) and an antibody to keratin 5 (green) in the right panel. Bars, 50 μm.

the epidermis and was apparent at the transition between the embryo ectoderm and the amnion of wild-type mice at 16.5 dpc (Fig. 6, B and C). To characterize the function of the epidermal ridge, we stained it for F-actin, phosphorylated MLC, and keratin 5 (Fig. 6 D). Intense phalloidin staining and phosphorylated MLC was detected in the epithelial layer covering the ridge of wild-type embryos. Both of these signals were absent in the epithelium of ROCK-I$^{-/-}$ embryos. These results indicate that specific actin bundles are localized in the epithelial cells of the umbilical ring. Together, these results suggest that the impaired closure of the umbilical ring in ROCK-I$^{-/-}$ embryos is due to failure of myosin phosphorylation and actin assembly in the epithelium at the site of formation of the epidermal ridge at the ectoderm–amnion transition.

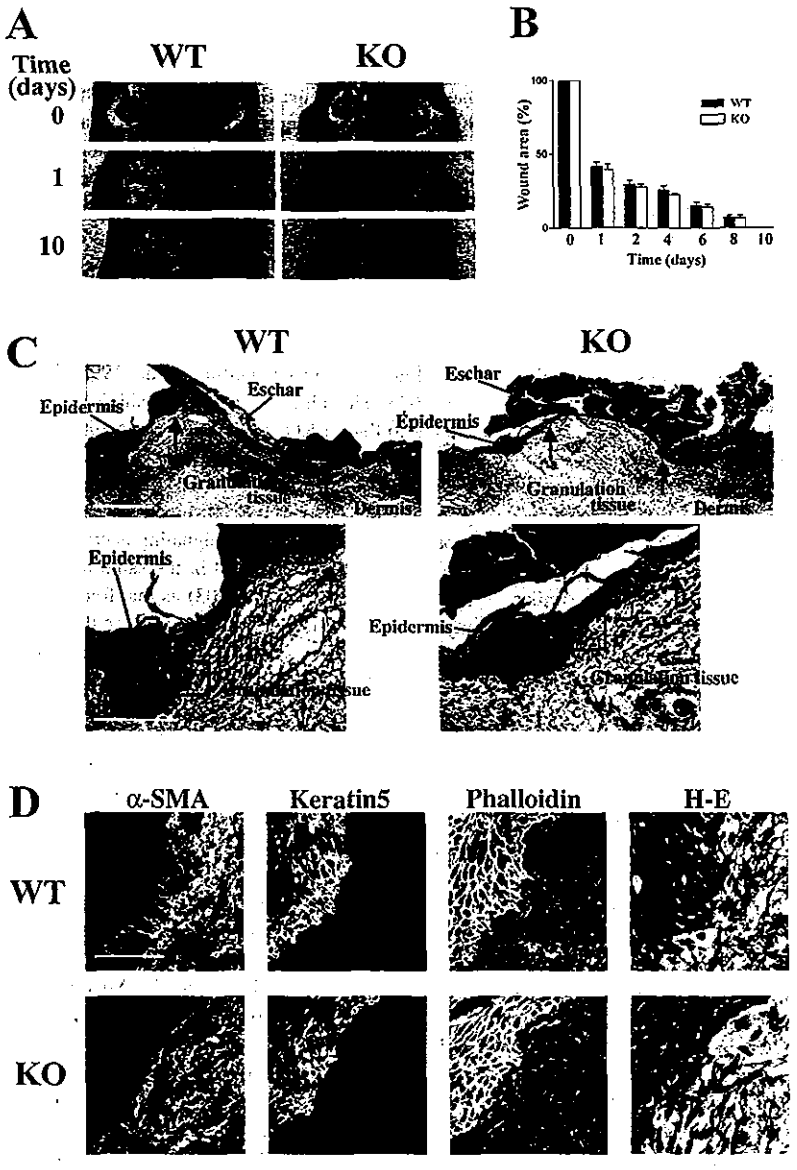

Figure 7. **Wound healing in adult wild-type and ROCK-I $^{-/-}$ mice.** (A) Adult wild-type or ROCK-I$^{-/-}$ mice were shaved on their backs and a 6-mm-diam cylinder of skin (full thickness) was punched out bilaterally. Healing of the wounds was monitored for 10 d. (B) Wound area was expressed as a percentage of the initial value. Quantitative data are means ± SEM (n = 8 wounds for each group). (C) Hematoxylin-eosin staining of the transverse sections of the wound on day 5 from wild-type (left) and ROCK-I$^{-/-}$ mice (right). Arrows indicate the foremost tips of the migrating epithelial sheet. Areas of the migrating epithelial sheet are enlarged in the bottom panels. Bars: (top) 500 μm; (bottom) 200 μm. (D) Staining of the wound edge. Serial sections of the wound from wild-type (top) and ROCK-I$^{-/-}$ (bottom) mice were stained with antibodies to α-SMA, keratin 5, phalloidin, and hematoxylin-eosin (H-E). The fields of view shown correspond to the regions boxed in C. Bar, 50 μm.

Wound healing in adult ROCK-I$^{-/-}$ mice

Finally, we examined the effect of ROCK-I deficiency on wound healing in adult mice. We punched out a full-thickness piece of skin and monitored closure of the excision wound in both wild-type and ROCK-I$^{-/-}$ animals. No apparent repair defect was detected in ROCK-I$^{-/-}$ mice, with wound healing after a time course similar to that observed in wild-type controls (Fig. 7, A and B). Histological examination of the wound on day 5 revealed that the epidermal edges of the wound migrate forward to cover the denuded wound surface in ROCK-I$^{-/-}$ mice as in wild-type controls (Fig. 7 C, arrows). In both groups, myofibroblasts expressing α-smooth muscle actin (α-SMA) were detected underneath the migrating epidermis in granulation tissue (Fig. 7 D). These myofibroblasts was similarly stained with phalloidin in the two groups. These results suggest that ROCK-I is not essential for migration of keratinocytes and appearance of myofibroblasts in adult wound healing process.

Discussion

We have disrupted the gene for ROCK-I, one of the two isoforms of ROCK, by homologous recombination in mice in order to elucidate the functions of this protein in vivo. Mice homozygous for the disrupted ROCK-I allele manifested the EOB and omphalocele phenotypes. Analysis of the molecular mechanisms responsible for these abnormalities has revealed an evolutionarily conserved role of ROCK-I in animal development.

ROCK-I–dependent assembly of actomyosin cables: conservation in mammalian eyelid closure and in *Drosophila* dorsal closure

Monitoring of the morphological changes associated with eyelid closure revealed that the extension of the eyelid epithelial sheet that occurs in wild-type embryos was markedly impaired in ROCK-I$^{-/-}$ mice. Staining with phalloidin and antibodies to phosphorylated MLC revealed the presence of thick actomyosin cables that course around the circumference of the eye and join neighboring cells together in the eyelid epithelial sheet of wild-type mice. This actomyosin structure was specifically lost in the eyelids of ROCK-I$^{-/-}$ mice. Given the functions of ROCK in actomyosin dynamics, these findings indicate that ROCK-I is activated in cells of the eyelid epithelial sheet, catalyzes MLC phosphorylation, and thereby triggers the cross-linking of actin filaments and the assembly of actomyosin bundles, the latter of which then contract and provide the driving force necessary for eyelid closure. The loss of such ROCK-I function is thus the likely cause of the EOB phenotype in ROCK-I$^{-/-}$ mice.

This process that we propose for eyelid closure is similar to that which underlies dorsal closure of the fly epidermis (Jacinto et al., 2002). In both instances, the epithelium extends as a sheet and actomyosin cables are present in these sheets. On the basis of the contribution of a MAPK cascade (see below) to both processes, Xia and Karin (2004) suggested the operation of an evolutionarily conserved mechanism both in dorsal closure in *Drosophila* and in eyelid closure in mammals. Consistent with this proposal and with our present findings, genetic analysis in *Drosophila* has implicated the Rho pathway in dorsal closure (Harden et al., 1999; Magie et al., 1999). Moreover, disruption of the *Drosophila* gene for the myosin binding subunit of myosin phosphatase resulted in impairment of dorsal closure (Mizuno et al., 2002). Given that the myosin binding subunit of myosin phosphatase is the major substrate of ROCK in its indirect regulation of phosphorylated MLC, this finding suggests the participation of ROCK in dorsal closure. Laser-ablation experiments have shown that the actin cables generate the contractile force responsible for movement of the epithelial sheet during dorsal closure, functioning in a manner analogous to a purse string (Kiehart et al., 2000; Hutson et al., 2003). Therefore, we propose that actomyosin cable in eyelid epithelial sheet contracts like a purse string, and thus drive the eyelid epithelial sheet movement forward as seen in dorsal closure. In addition to dorsal closure, purse stringlike actin assembly occurs at the margin of wounds in chick embryos, and experiments with C3 exoenzyme have indicated that Rho mediates this assembly (Brock et al., 1996; Wood et al., 2002). Therefore, it is likely that Rho–ROCK signaling also contributes to wound closure in chick embryos. Thus, ROCK-mediated assembly and contraction of actomyosin cables appears to be an evolutionarily conserved mechanism for tissue closure.

In contrast to the findings in chick embryos, we found that ROCK-I deficiency did not affect wound closure in adult mice. Wound healing in adult skin is a complex process. After wounding, a fibrin clot and then granulation tissue form in the wound, after which a sheet of keratinocytes migrates from the wound edges to repair the epidermal layer (Martin, 1997). This migration of the epithelium occurs by integrin-dependent extension of lamellipodia over the ECM. Failure of ROCK-I deficiency to block this process suggests that ROCK-I is not required for cell migration over ECM in adult skin. Consistent with this conclusion, an in vitro assay of wound healing with a monolayer of cultured keratinocytes revealed that keratinocytes derived from wild-type or ROCK-I$^{-/-}$ mice migrated in response to EGF stimulation in similar manners (unpublished data).

Role of ROCK-I in EGF signaling during eyelid closure

EGFR-deficient mice (Miettinen et al., 1995; Sibilia and Wagner, 1995; Threadgill et al., 1995) exhibit an EOB phenotype similar to that of ROCK-I$^{-/-}$ mice. In addition, mice deficient in TGF-α (Luetteke et al., 1993; Mann et al., 1993), an EGFR ligand, and mice deficient in Gab1 (Itoh et al., 2000), an adaptor molecule of the EGFR, also manifest the open-eye phenotype, suggesting that EGFR signaling is critical for eyelid closure. The EGFR is activated in the same region of the eyelid epithelial sheet (Li et al., 2003) as that found to contain actomyosin cables in the present study. Given that Rho is activated by EGFR signaling in cultured cells (Ridley and Hall, 1992), Rho–ROCK signaling likely functions downstream of the EGFR in eyelid closure. We have now shown that EGF activates Rho and induces both phosphorylation of MLC and formation of stress fibers in a ROCK-I–dependent manner in primary mouse keratinocytes, supporting the notion that ROCK-I functions in induction of formation of the actomyosin cables in the eyelid epithelial sheet.

We also examined whether the Rho–ROCK pathway might play a role in EGFR signaling other than that which leads to the formation of actomyosin cables. Knockout mouse studies have implicated a MAPK cascade in EGF signaling during eyelid closure. For example, MEKK1-deficient mice exhibit the EOB phenotype (Zhang et al., 2003). JNK1$^{+/-}$/JNK2$^{-/-}$ mice (Weston et al., 2004) as well as mice with keratinocyte-specific knockout of c-Jun (Li et al., 2003; Zenz et al., 2003) are also defective in eyelid closure. In all of these mutant mice, the EOB phenotype is associated with reduced expression of the EGFR ligands EGF or heparin-binding EGF, indicating the presence of a positive feedback loop. The recent observation that RhoA stimulates the expression of c-Jun by activating JNK (Marinissen et al., 2004) led us to examine the possible role of ROCK-I in this signaling cascade. However, JNK activation and phosphorylation of c-Jun were not altered in ROCK-I$^{-/-}$ keratinocytes, excluding a role for ROCK-I in this MAPK cascade. On the basis of these various observations, we propose the model shown in Fig. 5 F for the role of ROCK-I in the EGFR signaling associated with eyelid closure.

Umbilical ring closure is mediated by ROCK-I–dependent actin assembly

A reduced level of MLC phosphorylation and consequent failure of actomyosin assembly in the epithelium may also explain the omphalocele phenotype of ROCK-I$^{-/-}$ neonates. Accumu-

lation of filamentous-actin and MLC phosphorylation were observed in the epithelial cells at the ectoderm–amnion transition that formed a ridge-shaped structure encircling the umbilical ring in wild-type mouse embryos. Neither such filamentous-actin accumulation nor MLC phosphorylation was detected and the epidermal ridge was not formed in ROCK-I$^{-/-}$ embryos. In contrast, although omphalocele can be caused by defects or malformation of the ventral body wall itself (Eggenschwiler et al., 1997; Zhang et al., 1997; Brewer and Williams, 2004), this structure was intact in ROCK-I$^{-/-}$ embryos. These results indicate that ROCK-I$^{-/-}$ embryos are defective in the final step of umbilical ring closure, which we propose is executed by ROCK-I–mediated actomyosin contraction of the epithelium in the epidermal ridge. In contrast to the EOB phenotype, omphalocele is not observed in mice defective in EGFR signaling. Moreover, the extents of the EOB phenotype and of omphalocele were not correlated in ROCK-I$^{-/-}$ embryos, suggesting that the upstream signaling in umbilical closure differs from that in eyelid closure. The omphalocele phenotype of the ROCK-I$^{-/-}$ mice is reminiscent of that of human neonatal omphalocele, for which failure of umbilical ring closure is proposed as a major cause. The incidence of human omphalocele has been estimated as 1 in 4,000–7,000 live births (Weber et al., 2002). Characterization of the detailed mechanism of the failure of umbilical ring closure in ROCK-I$^{-/-}$ mice may thus provide insight into the pathophysiology of omphalocele and its treatment in humans.

Further considerations

Given the importance of ROCK in Rho signaling, the phenotype of ROCK-I$^{-/-}$ mice described in the present study as well as that of ROCK-II$^{-/-}$ mice we described previously (Thumkeo et al., 2003) might be considered milder than expected. Both types of knockout mice manifest perinatal problems, but those that survive develop in an apparently normal manner to adulthood. In addition, in the present study, some ROCK-I$^{-/-}$ embryos exhibited partial extension of the eyelid epithelial sheet and associated actin bundling. EGF induced a low level of stress fiber formation in ROCK-I$^{-/-}$ keratinocytes, and this effect was abolished by Y-27632, suggesting a contribution, albeit little, by ROCK-II in the same process. Consistently, we recently found that a substantial proportion of ROCK-II$^{-/-}$ embryos also exhibited the EOB phenotype and omphalocele (unpublished data). These results suggest that ROCK-I and ROCK-II function in a redundant manner, and indicate a possibility that each is able to compensate functionally for the loss of the other in most systems without up-regulation except the tissues such as the placenta (Thumkeo et al., 2003) and the eyelid and umbilical ring (this study). The generation of double knockout mice deficient in both ROCK-I and ROCK-II should therefore provide further insight into the role of the ROCK family of kinases in development.

Materials and methods

Generation of ROCK-I–deficient mice

Several clones containing various portions of the ROCK-I gene were isolated from a 129/SvJ lambda FIXII genomic library (Stratagene). A 1.1-kb fragment containing the first 3 bp and 5′ flanking region of exon 3 was generated by PCR with a 3.8-kb genomic DNA fragment containing exons 3 and 4 as the template and with a forward primer containing a SmaI site and a reverse primer containing a ClaI site. The amplified fragment was subcloned as a short arm into pBluescript SK+ (Stratagene). The plasmid DNA was cut with ClaI and SalI and fused with a ClaI–SalI fragment containing the β-galactosidase gene. The multicloning site of pKOScrambler915 (Stratagene) was modified to contain the restriction enzyme sites RsrII–EcoRI–XhoI–AscI–SacII–ClaI–SmaI–BglII–AvrII–SalI–NotI, yielding mpKO915. The latter plasmid was cut with AscI, and the AscI fragment of the phosphoglycerate kinase promoter-neomycin resistance (neo) cassette was introduced at this site. The diphtheria toxin A gene was then inserted at the RsrII site of the mpKO915 plasmid, after which the SmaI–SalI fragment containing the short arm of the ROCK-I gene and the β-galactosidase gene from pBluescript SK+ was subcloned into the EcoRI–XhoI site. Finally, a 7.8-kb EcoRV–NheI fragment of genomic DNA of ROCK-I was inserted as the long arm into the SmaI site of the vector to generate the targeting construct (Fig. 1 A). The targeting vector was linearized with NotI and introduced into embryonic stem cells (line RW4; Genome System) by electroporation. G418-resistant clones were isolated, and homologous recombination was verified in three clones by PCR-based genotyping. Cells of each of the three clones were injected into blastocysts, and the chimeric male offspring obtained were mated with C57BL/6N females. ROCK-I$^{+/-}$ heterozygous mice were then intercrossed to produce ROCK-I$^{-/-}$ homozygotes. Mice studied in the present work had been backcrossed to the C57BL/6N strain for more than five generations. The morning of the day on which a vaginal plug was detected was designated as 0.5 dpc. All animal experiments were approved by the Committee on Animal Research of Kyoto University Faculty of Medicine and were performed according to the guidelines for the protection of experimental animals of Kyoto University, Kyoto, Japan.

Genotyping

Genotyping was performed by Southern blot or PCR analysis with genomic DNA isolated from embryonic stem cells, embryonic visceral yolk sacs, or the tail of mice. For Southern analysis, 10 μg of genomic DNA were digested with BglII for 12 h at 37°C, and the resulting fragments were fractionated by electrophoresis on a 0.7% agarose gel, transferred to a Hybond-N$^+$ nylon membrane (Amersham Biosciences), and subjected to hybridization overnight at 42°C in hybridization buffer (Ultrasensitive Hybridization buffer; Ambion) with the external probe (Fig. 1 A) that had been randomly labeled with α-[^{32}P]dCTP (1×10^6 to 2×10^6 cpm/ml) with the use of Ready-To-Go DNA Labeling Beads (Amersham Biosciences). For PCR analysis, the primers were 5′-CACTACAATCAAGTAAGCTTCATCC-3′ (forward primer for the wild-type and targeted allele), 5′-GCTGAGCAGCTTCATAGCATAAACC-3′ (reverse primer for the wild-type allele), and 5′-GACCAGACCGTTCATACAGAACTGG-3′ (reverse primer for the targeted allele).

Production of antibodies to mouse ROCK-I

A GST fusion protein of fragment 1b of mouse ROCK-I (amino acids 400–662) was produced in *Escherichia coli* BL21 cells, and purified with the use of glutathione-Sepharose 4B beads (Amersham Biosciences). GST was cleaved, and ROCK-I (1b) was used as the antigen and injected into rabbits. Specific antibodies to mouse ROCK-I were then affinity purified from serum with the use of ROCK-I (1b) immobilized on CNBr beads (Amersham Biosciences).

Immunoblot analysis

The entire brain of adult mice or confluent monolayers of primary keratinocytes were homogenized, and used for immunoblotting as described previously (Thumkeo et al., 2003) with antibodies to either ROCK-I, ROCK-II (H-85; Santa Cruz Biotechnology, Inc.), β-tubulin (TUB 2.1; Sigma-Aldrich), phosphorylated MLC (Matsumura et al., 1998), MLC (A-10; Santa Cruz Biotechnology, Inc.), phosphorylated JNK (Promega), JNK (BD Biosciences), phosphorylated c-Jun (Cell Signaling Technology), or c-Jun (H-79; Santa Cruz Biotechnology, Inc.).

Whole-mount staining for β-galactosidase

Embryos isolated at 13.5 or 15.5 dpc were processed for whole-mount β-galactosidase staining as described previously (Thumkeo et al., 2003).

Histological and immunofluorescence analyses

Samples were fixed in 10% formaldehyde, dehydrated with a graded series of ethanol solutions, and embedded in paraffin. 8-μm sections were prepared, subjected to removal of paraffin by immersion in xylene, rehy-

drated, and stained with hematoxylin-eosin. The samples were embedded in Tissue Tek OCT compound (Sakura) and frozen on dry ice. Cryostat sections (12 μm) were prepared and subjected to indirect immunofluorescence analysis with antibodies to either phosphorylated MLC (Matsumura et al., 1998), myosin (BT-561; Biomedical Technologies), keratin 5 or keratin 10 (BabCo), keratin 6 (McGowan and Coulombe, 1998), Ki67 (Novocastra), or α-SMA (1A4; Sigma-Aldrich). Antibody to keratin 6 was a gift from B.A. Coulombe (Johns Hopkins University of Medicine, Baltimore, MD). Immunocomplexes were detected with Alexa Fluor 488–conjugated donkey antibodies to rabbit or mouse IgG (Molecular Probes). TOPRO-3 iodide and phalloidin labeled with either Oregon green or Texas red (Molecular Probes) were used for staining of nuclei and filamentous actin, respectively. Primary keratinocytes were fixed with 4% PFA for 15 min at RT, permeabilized for 5 min with PBS containing 0.1% Triton X-100, and stained for filamentous actin with Oregon green phalloidin. Specimens were examined with the LSM 510 confocal microscope, at RT, with both 40× (Plan-Neofluor; NA 1.3) and 63× (Plan-Apochromat; NA 1.4) objective lens. Images were acquired with LSM 510 AIM software (Carl Zeiss MicroImaging, Inc.). All pseudo-color representations were assembled using Adobe Photoshop version 6.0 for illustrative purpose only.

Scanning electron microscopy

The head of embryos at 14.5–16.5 dpc was fixed in 0.1 M sodium phosphate buffer, pH 7.4, containing 1% glutaraldehyde and 4% formaldehyde, washed with 0.1 M sodium phosphate buffer containing 0.1 M sucrose, and dehydrated with a graded series of ethanol solutions. Specimens were then dried and sputter coated according to standard procedures before examination with an S4700 scanning electron microscope (Hitachi).

Whole-mount phalloidin staining

Eyelids isolated together with the skin around the eye from embryos at 15.5 or 16.0 dpc were fixed in 4% PFA for 30 min, washed with PBS, incubated for 1 h with 200 μl of Oregon green phalloidin diluted 1:50 in PBS containing 0.2% Triton X-100, and washed five times with the PBS Triton X-100 solution. Specimens were examined under a fluorescence microscope (model BX50; Olympus) equipped with a charge-coupled device camera (model DP-70; Olympus) as well as with the LSM 510 confocal imaging system (Carl Zeiss MicroImaging, Inc.).

Primary culture of keratinocytes

Primary culture of mouse keratinocytes was performed as described previously (Sano et al., 1999). For pull-down assay, keratinocytes were lysed in pull-down lysis buffer (Upstate Biotechnology), and the lysate was subjected to the pull-down assay using a GST fusion protein containing the Rho binding domain of Rhotekin (Upstate Biotechnology). For BrdU incorporation, keratinocytes were cultured for 24 h with EGF (10 ng/ml), after which BrdU (Roche) was added to the culture medium at 10 μM. After further incubation for 1 h, the cells were fixed and stained with antibodies to BrdU (BMC 9318; Roche).

We thank P.A. Coulombe for polyclonal antibodies to keratin 6; S. Itami and Y. Sumikawa for protocols and advice on primary culture of keratinocytes; M. Fujioka for scanning electron microscopy; Y. Andou for help with preparation of the polyclonal antibodies to ROCK1; T. Fujiwara, K. Nonomura, Y. Che, and K. Hamajima for technical assistance; and T. Arai and Y. Kitagawa for secretarial assistance.

This work was supported in part by a grant-in-aid for Specially Promoted Research from the Ministry of Education, Culture, Sports, Science, and Technology of Japan, a grant from the Organization for Pharmaceutical Safety and Research, and a grant from Mitsubishi Pharma Corporation. The authors declare that they have no competing financial interests.

Submitted: 29 November 2004
Accepted: 3 February 2005

References

Amano, M., Y. Fukata, and K. Kaibuchi. 2000. Regulation and functions of Rho-associated kinase. *Exp. Cell Res.* 261:44–51.

Brewer, S., and T. Williams. 2004. Loss of AP-2alpha impacts multiple aspects of ventral body wall development and closure. *Dev. Biol.* 267:399–417.

Brock, J., K. Midwinter, J. Lewis, and P. Martin. 1996. Healing of incisional wounds in the embryonic chick wing bud: characterization of the actin purse-string and demonstration of a requirement for Rho activation. *J. Cell Biol.* 135:1097–1107.

Eggenschwiler, J., T. Ludwig, P. Fisher, P.A. Leighton, S.M. Tilghman, and A. Efstratiadis. 1997. Mouse mutant embryos overexpressing IGF-II exhibit phenotypic features of the Beckwith-Wiedemann and Simpson-Golabi-Behmel syndromes. *Genes Dev.* 11:3128–3142.

Etienne-Manneville, S., and A. Hall. 2002. Rho GTPases in cell biology. *Nature.* 420:629–635.

Findlater, G.S., R.D. McDougall, and M.H. Kaufman. 1993. Eyelid development, fusion and subsequent reopening in the mouse. *J. Anat.* 183:121–129.

Fuchs, E. 1996. The cytoskeleton and disease: genetic disorders of intermediate filaments. *Annu. Rev. Genet.* 30:197–231.

Harden, N., M. Ricos, Y.M. Ong, W. Chia, and L. Lim. 1999. Participation of small GTPases in dorsal closure of the *Drosophila* embryo: distinct roles for Rho subfamily proteins in epithelial morphogenesis. *J. Cell Sci.* 112:273–284.

Hutson, M.S., Y. Tokutake, M.S. Chang, J.W. Bloor, S. Venakides, D.P. Kiehart, and G.S. Edwards. 2003. Forces for morphogenesis investigated with laser microsurgery and quantitative modeling. *Science.* 300:145–149.

Itoh, M., Y. Yoshida, K. Nishida, M. Narimatsu, M. Hibi, and T. Hirano. 2000. Role of Gab1 in heart, placenta, and skin development and growth factor- and cytokine-induced extracellular signal-regulated kinase mitogen-activated protein kinase activation. *Mol. Cell. Biol.* 20:3695–3704.

Jacinto, A., S. Woolner, and P. Martin. 2002. Dynamic analysis of dorsal closure in *Drosophila*: from genetics to cell biology. *Dev. Cell.* 3:9–19.

Kaufman, M.H. 2002. The Atlas of Mouse Development. Academic Press, London. 525 pp.

Kiehart, D.P., C.G. Galbraith, K.A. Edwards, W.L. Rickoll, and R.A. Montague. 2000. Multiple forces contribute to cell sheet morphogenesis for dorsal closure in *Drosophila*. *J. Cell Biol.* 149:471–490.

Li, G., C. Gustafson-Brown, S.K. Hanks, K. Nason, J.M. Arbeit, K. Pogliano, R.M. Wisdom, and R.S. Johnson. 2003. c-Jun is essential for organization of the epidermal leading edge. *Dev. Cell.* 4:865–877.

Lueteke, N.C., T.H. Qiu, R.L. Peiffer, P. Oliver, O. Smithies, and D.C. Lee. 1993. TGF alpha deficiency results in hair follicle and eye abnormalities in targeted and waved-1 mice. *Cell.* 73:263–278.

Maekawa, M., T. Ishizaki, S. Boku, N. Watanabe, A. Fujita, A. Iwamatsu, T. Obinata, K. Ohashi, K. Mizuno, and S. Narumiya. 1999. Signaling from Rho to the actin cytoskeleton through protein kinases ROCK and LIM-kinase. *Science.* 285:895–898.

Magie, C.R., M.R. Meyer, M.S. Gorsuch, and S.M. Parkhurst. 1999. Mutations in the Rho1 small GTPase disrupt morphogenesis and segmentation during early *Drosophila* development. *Development.* 126:5353–5364.

Mann, G.B., K.J. Fowler, A. Gabriel, E.C. Nice, R.L. Williams, and A.R. Dunn. 1993. Mice with a null mutation of the TGF alpha gene have abnormal skin architecture, wavy hair, and curly whiskers and often develop corneal inflammation. *Cell.* 73:249–261.

Marinissen, M.J., M. Chiariello, T. Tanos, O. Bernard, S. Narumiya, and J.S. Gutkind. 2004. The small GTP-binding protein RhoA regulates c-jun by a ROCK-JNK signaling axis. *Mol. Cell.* 14:29–41.

Martin, P. 1997. Wound healing-aiming for perfect skin regeneration. *Science.* 276:75–81.

Martin, P., and S.M. Parkhurst. 2004. Parallels between tissue repair and embryo morphogenesis. *Development.* 131:3021–3034.

Matsumura, F., S. Ono, Y. Yamakita, G. Totsukawa, and S. Yamashiro. 1998. Specific localization of serine 19 phosphorylated myosin II during cell locomotion and mitosis of cultured cells. *J. Cell Biol.* 140:119–129.

Mazzalupo, S., and P.A. Coulombe. 2001. A reporter transgene based on a human keratin 6 gene promoter is specifically expressed in the periderm of mouse embryos. *Mech. Dev.* 100:65–69.

McGowan, K.M., and P.A. Coulombe. 1998. Onset of keratin 17 expression coincides with the definition of major epithelial lineages during skin development. *J. Cell Biol.* 143:469–486.

Miettinen, P.J., J.E. Berger, J. Meneses, Y. Phung, R.A. Pedersen, Z. Werb, and R. Derynck. 1995. Epithelial immaturity and multiorgan failure in mice lacking epidermal growth factor receptor. *Nature.* 376:337–341.

Mizuno, T., K. Tsutsui, and Y. Nishida. 2002. *Drosophila* myosin phosphatase and its role in dorsal closure. *Development.* 129:1215–1223.

Narumiya, S. 1996. The small GTPase Rho: cellular functions and signal transduction. *J. Biochem. (Tokyo).* 120:215–228.

Ridley, A.J., and A. Hall. 1992. The small GTP-binding protein rho regulates the assembly of focal adhesions and actin stress fibers in response to growth factors. *Cell.* 70:389–399.

Riento, K., and A.J. Ridley. 2003. Rocks: multifunctional kinases in cell behaviour. *Nat. Rev. Mol. Cell Biol.* 4:446–456.

Sano, S., S. Itami, K. Takeda, M. Tarutani, Y. Yamaguchi, H. Miura, K. Yoshikawa, S. Akira, and J. Takeda. 1999. Keratinocyte-specific ablation of Stat3 exhibits impaired skin remodeling, but does not affect skin

morphogenesis. *EMBO J.* 18:4657–4668.

Sibilia, M., and E.F. Wagner. 1995. Strain-dependent epithelial defects in mice lacking the EGF receptor. *Science.* 269:234–238.

Threadgill, D.W., A.A. Dlugosz, L.A. Hansen, T. Tennenbaum, U. Lichti, D. Yee, C. LaMantia, T. Mourton, K. Herrup, R.C. Harris, et al. 1995. Targeted disruption of mouse EGF receptor: effect of genetic background on mutant phenotype. *Science.* 269:230–234.

Thumkeo, D., J. Keel, T. Ishizaki, M. Hirose, K. Nonomura, H. Oshima, M. Oshima, M.M. Taketo, and S. Narumiya. 2003. Targeted disruption of the mouse rho-associated kinase 2 gene results in intrauterine growth retardation and fetal death. *Mol. Cell. Biol.* 23:5043–5055.

Uehata, M., T. Ishizaki, H. Satoh, T. Ono, T. Kawahara, T. Morishita, H. Tamakawa, K. Yamagami, J. Inui, M. Maekawa, and S. Narumiya. 1997. Calcium sensitization of smooth muscle mediated by a Rho-associated protein kinase in hypertension. *Nature.* 389:990–994.

Weber, T.R., M. Au-Fliegner, C.D. Downard, and S.J. Fishman. 2002. Abdominal wall defects. *Curr. Opin. Pediatr.* 14:491–497.

Weston, C.R., A. Wong, J.P. Hall, M.E. Goad, R.A. Flavell, and R.J. Davis. 2004. The c-Jun NH2-terminal kinase is essential for epidermal growth factor expression during epidermal morphogenesis. *Proc. Natl. Acad. Sci. USA.* 101:14114–14119.

Wood, W., A. Jacinto, R. Grose, S. Woolner, J. Gale, C. Wilson, and P. Martin. 2002. Wound healing recapitulates morphogenesis in *Drosophila* embryos. *Nat. Cell Biol.* 4:907–912.

Xia, Y., and M. Karin. 2004. The control of cell motility and epithelial morphogenesis by Jun kinases. *Trends Cell Biol.* 14:94–101.

Zenz, R., H. Scheuch, P. Martin, C. Frank, R. Eferl, L. Kenner, M. Sibilia, and E.F. Wagner. 2003. c-Jun regulates eyelid closure and skin tumor development through EGFR signaling. *Dev. Cell.* 4:879–889.

Zhang, L., W. Wang, Y. Hayashi, J.V. Jester, D.E. Birk, M. Gao, C.Y. Liu, W.W. Kao, M. Karin, and Y. Xia. 2003. A role for MEK kinase 1 in TGF-beta/activin-induced epithelium movement and embryonic eyelid closure. *EMBO J.* 22:4443–4454.

Zhang, P., N.J. Liegeois, C. Wong, M. Finegold, H. Hou, J.C. Thompson, A. Silverman, J.W. Harper, R.A. DePinho, and S.J. Elledge. 1997. Altered cell differentiation and proliferation in mice lacking p57KIP2 indicates a role in Beckwith-Wiedemann syndrome. *Nature.* 387:151–158.

Molecular Cell, Vol. 13, 511–522, February 27, 2004, Copyright ©2004 by Cell Press

The Core FH2 Domain of Diaphanous-Related Formins Is an Elongated Actin Binding Protein that Inhibits Polymerization

Atsushi Shimada,[1,6] Miklós Nyitrai,[2,3,6] Ingrid R. Vetter,[1] Dorothee Kühlmann,[1] Beáta Bugyi,[4] Shuh Narumiya,[5] Michael A. Geeves,[2] and Alfred Wittinghofer[1,*]
[1]Max-Planck Institut für Molekulare Physiologie
Otto Hahn Strasse 11
D-44227 Dortmund
Germany
[2]Department of Biosciences
University of Kent
Canterbury, Kent CT2 7NJ
United Kingdom
[3]Research Group for Fluorescence Spectroscopy
Office for Academy Research Groups Attached to Universities and Other Institutions
[4]Department of Biophysics
Faculty of Medicine
University of Pécs
H-7601 Pécs
Hungary
[5]Department of Pharmacology
Kyoto University Faculty of Medicine
Yoshida, Sakyo-ku, Kyoto 606-8501
Japan

Summary

Diaphanous-related formins (Drf) are activated by Rho GTP binding proteins and induce polymerization of unbranched actin filaments. They contain three formin homology domains. Evidence as to the effect of formins on actin polymerization were obtained using FH2/FH1 constructs of various length from different Drfs. Here we define the core FH2 domain as a proteolytically stable domain of approximately 338 residues. The monomeric FH2 domains from mDia1 and mDia3 inhibit polymerization of actin and can bind in a 1:1 complex with F-actin at micromolar concentrations. The X-ray structure analysis of the domain shows an elongated, crescent-shaped molecule consisting of three helical subdomains. The most highly conserved regions of the domain span a distance of 75 Å and are both required for barbed-end inhibition. A construct containing an additional 72 residue linker has dramatically different properties: It oligomerizes and induces actin polymerization at subnanomolar concentration.

Introduction

The formin proteins play important roles in many different cellular processes such as cytokinesis, vesicular trafficking, and the maintenance of cell polarity by regulating actin and microtubule cytoskeletons (Wallar and Alberts, 2003). They have in common a poly-proline-rich formin homology-1 (FH1) domain, which binds profilin and protein-interacting modules such as the SH3 or WW domain (Wallar and Alberts, 2003). They also contain a FH2 domain of undefined length and structure, usually in tandem with FH1.

Diaphanous-related formins (Drfs) such as the (mammalian) mDia proteins (mDia 1, 2, and 3) have an additional GTPase binding domain (GBD) which is involved in binding the GTP-bound form of Rho proteins (Evangelista et al., 1997; Kohno et al., 1996; Watanabe et al., 1997), connected to the FH3 domain of undefined length and structure. In Drfs the activity of the protein is regulated by the C-terminal diaphanous autoregulatory domain (DAD), which binds to the GBD and inhibits biological activity (Watanabe et al., 1999; Alberts, 2001). While mDia is directly mediating Rho-induced actin reorganization (Watanabe et al., 1997, 1999), it has also been implicated in microtubule alignment and stabilization (Ishizaki et al., 2001; Palazzo et al., 2001).

It has been shown that the FH2 domain plays an important role for the function of formin family proteins. Mutations in the FH2 domain abolish both the bundling of actin filaments and the alignment of microtubules induced by an active mutant of mDia1 lacking the GBD (Ishizaki et al., 2001). A close link exists between the control of cytoskeletal organization and the transcription factor serum response factor (SRF), where SRF is negatively regulated by the actin monomer pool in the cells (Posern et al., 2002; Sotiropoulos et al., 1999). For this system it has been shown in cell culture studies that the lysophosphatidic acid (LPA)-induced activation of SRF is mediated by mDia and in particular by the region encompassing the FH2 domains (Copeland and Treisman, 2002).

Fragments of various length covering the FH2 domains of formins exhibited activity to nucleate actin in vitro (Pruyne et al., 2002; Sagot et al., 2002b; Pring et al., 2003; Kovar et al., 2003; Li and Higgs, 2003). All the FH2 fragments from either *S. cerevisiae* Bni1p, *S. pombe* Cdc12p, or mDia1 used in the previous studies (Figure 1A) have in common the property to affect barbed-end kinetics of F-actin via a complete or partial capping mechanism. Although the FH1 domain is dispensable for in vitro actin polymerization induced by the FH2 domain, it modulates the activity of the FH2 domain by its interaction with profilin (Pruyne et al., 2002; Sagot et al., 2002b; Kovar et al., 2003; Li and Higgs, 2003). It has been also proposed that these fragments form a dimer or higher oligomers, which is likely related to their function (Li and Higgs, 2003; Zigmond et al., 2003; Takeya and Sumimoto, 2003).

The exact domain boundaries of the FH2 domain and the minimal functional unit for actin nucleation were not clear. To dissect and structurally define the domain boundaries of these proteins and to understand the contribution of the core FH2 domain (as defined in this article) to actin polymerization, we isolated and characterized proteolytically stable FH2 domain fragments from both mouse mDia1 and mDia3. The 338 residue fragment did not nucleate, but did inhibit, actin polymerization. We also show that the additional presence of the linker region between the FH1 and FH2 domain is

*Correspondence: alfred.wittinghofer@mpi-dortmund.mpg.de
[6]These authors contributed equally to this work.

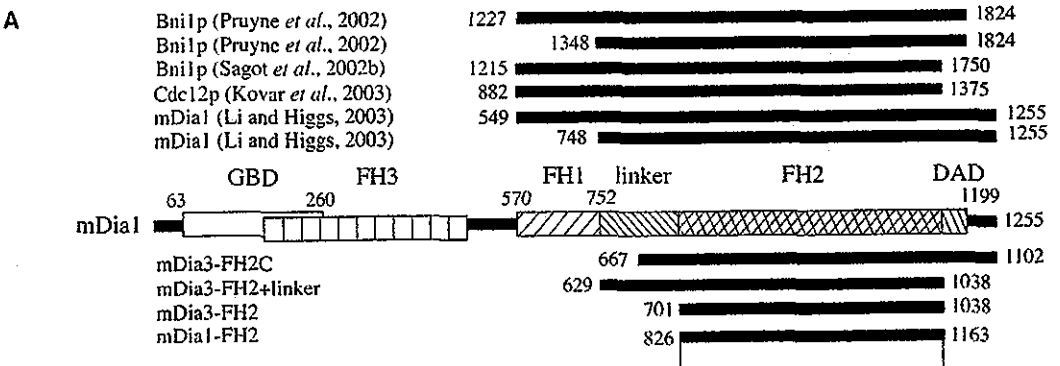
A
Bni1p (Pruyne et al., 2002)
Bni1p (Pruyne et al., 2002)
Bni1p (Sagot et al., 2002b)
Cdc12p (Kovar et al., 2003)
mDia1 (Li and Higgs, 2003)
mDia1 (Li and Higgs, 2003)
1227
1824
1348
1824
1215
1750
882
1375
549
1255
748
1255
GBD
FH3
FH1
linker
FH2
DAD
63
260
570
752
1199
mDia1
1255
mDia3-FH2C
667
1102
mDia3-FH2+linker
629
1038
mDia3-FH2
701
1038
mDia1-FH2
826
1163

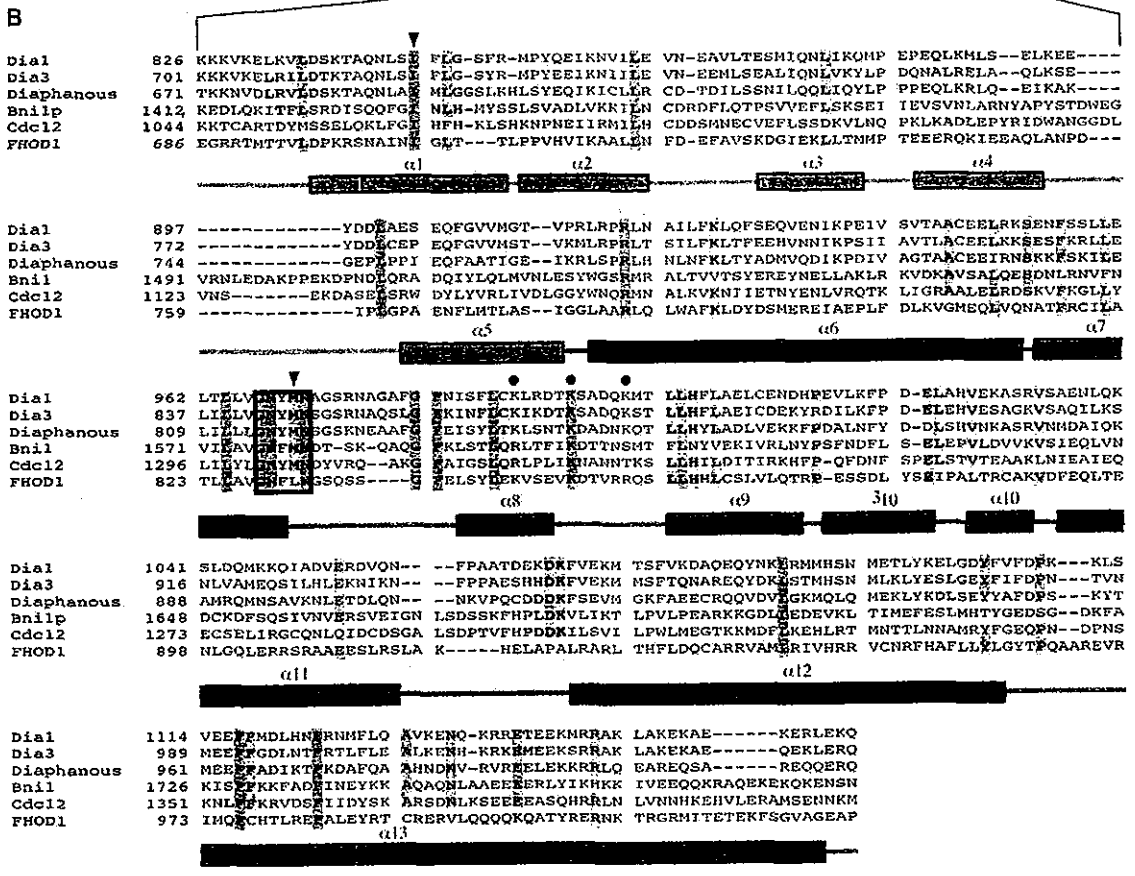
B
Dia1 826 KKKVKELKVLDSKTAQNLSS FLG-SFR-MPYQEIKNVILE VN-EAVLTESMIQNLIKQHP EPEQLKMLS--ELKEE----
Dia3 701 KKKVKELRILDTKTAQNLSS FLG-SYR-MPYEEIKNIILE VN-EEMLSEALIQNLVKYLP DQNALRELA--QLKSE----
Diaphanous 671 TKKNVDLRVLDSKTAQNLAS MLGGSLKHLSYEQIKICLER CD-TDILSSNILQQLIQYLP PPEQLKRLQ--EIKAK----
Bni1p 1412 KEDLQKITFLSRDISQQFGL NLH-MYSSLSVADLVKRILN CDRDFLQTPSVVEFLSKSEI IEVSVNLARNYAPYSTDWEG
Cdc12 1044 KKTCARTDYMSSELQKLFGL HFH-KLSHKNPNEIIRMILH CDDSMNECVEFLSSDKVLNQ PKLKADLEPYRIDWANGGDL
FHOD1 686 EGRRTMTTVLDPKRSNAINT GLT---TLPPVHVIKAALEN FD-EFAVSKDGIEKLLTMMP TEEERQKIEEAQLANPD---
α1 α2 α3 α4
Dia1 897 ----------YDDEAES EQFGVVMGT--VPRLRPRLN AILFKLQFSEQVENIKPEIV SVTAACEELRKSENFSSLLE
Dia3 772 ----------YDDECEP EQFGVVMST--VKMLRPRLT SILFKLTFEEHVNNIKPSII AVTLACEELKKSESFKRLLE
Diaphanous 744 ----------GEPLPPI EQFAATIGE--IKRLSPRLH NLNFKLTYADMVQDIKPDIV AGTAACEEIRNSKKFSKILE
Bni1 1491 VRNLEDAKPPEKDPNDLQRA DQIYLQLMVNLESYWGSRMR ALTVVTSYEREYNELLAKLR KVDKAVSALQEHDNLRNVFN
Cdc12 1123 VNS--------EKDASELSRW DYLYVRLIVDLGGYWNQRMN ALKVKNIIETNYENLVRQTK LIGRAALELRDSKVFKGLLY
FHOD1 759 ----------IPEGPA ENFLMTLAS--IGGLAARLQ LWAFKLDYDSMEREIAEPLF DLKVGMEQLVQNATERCILA
α5 α6 α7
Dia1 962 LTELVNYMKAGSRNAGAFG ENISFLCKLRDTKSADQKMT LLHFLAELCENDHPEVLKFP D-ELAHVEKASRVSAENLQK
Dia3 837 LIELVNYMKSGSRNAQSLG EKINFLCKIKDTKSADQKST LLHFLAEICDEKYRDILKFP D-ELEHVESAGKVSAQILKS
Diaphanous 809 LIELLDYMKSGSKNEAAFG EEISYLTKLSNTKDADNKQT LLHYLADLVEKKFPDALNFY D-DLSHVNKASRVNMDAIQK
Bni1 1571 VIEAVDFFKDT-SK-QAQG EKLSTLQRLTFIKDTTNSMT FENYVEKIVRLNYPSFNDFL S-ELEPVLDVVKVSIEQLVN
Cdc12 1296 LIEYLNYMKDYVRQ--AKG EAIGSLQRLPLIKNANNTKS LLHILDITTRKHFP-QFDNF SPELSTVTEAAKLNIEAIEQ
FHOD1 823 TLEAVDFFLMGSQSS----G EELSYLEKVSEVKDTVRRQS LLHHLCSLVLQTRE-ESSDL YSEIPALTRCAKVDFEQLTE
α8 α9 310 α10
Dia1 1041 SLDQMKKQIADVERDVQN-- --FPAATDEKDKFVEKM TSFVKDAQEQYNKERMMHSN METLYKELGDYFVFDEK---KLS
Dia3 916 NLVAMEQSILHLEKNIKN-- --FPPAESHHDKFVEKM MSFTQNAREQYDKESTMHSN MLKLYESLGEYFIFDEN---TVN
Diaphanous 888 AMRQMNSAVKNLETDLQN-- --NKVPQCDDDKFSEVM GKFAEECRQQVDVLGKMQLQ MEKLYKDLSEYYAFDES---KYT
Bni1p 1648 DCKDFSQSIVNVERSVEIGN LSDSSKFHPLDKVLIKT LPVLPEARKKGDLLEDEVKL TIMEFESLMHTYGEDSG--DKFA
Cdc12 1273 ECSELIRGCQNLQIDCDSGA LSDPTVFHPDDKILSVI LPWLMEGTKKMDFLKEHLRT MNTTLNNAMRYFGEQFN--DPNS
FHOD1 898 NLGQLERRSRAAEESLRSLA K-----HELAPALRARL THFLDQCARRVAMGRIVHRR VCNRFHAFLLYLGYTFQAARFVR
α11 α12
Dia1 1114 VEEFFMDLHNFRNMFLQ AVKENQ-KRRETEEKMRRAK LAKEKAE------KERLEKQ
Dia3 989 MEEFFGDLNTFRTLFLE ALKENH-KRKEMEEKSRRAK LAKEKAE------QEKLERQ
Diaphanous 961 MEEFFADIKTFKDAFQA AHNDMV-RVREELEKKRRLQ EAREQSA------REQQERQ
Bni1 1726 KISFFKKFADFINEYKK AQAQNLAAEEERLYIKHKK IVEEQQKRAQEKEKQKENSN
Cdc12 1351 KNLFFKRVDSFIIDYSK ARSDNLKSEEEEASQHRRLN LVNNHKEHVLERAMSENNKM
FHOD1 973 IMQECHTLREFALEYRT CRERVLQQQQKQATYRERNK TRGRMITETEKFSGVAGEAP
α13

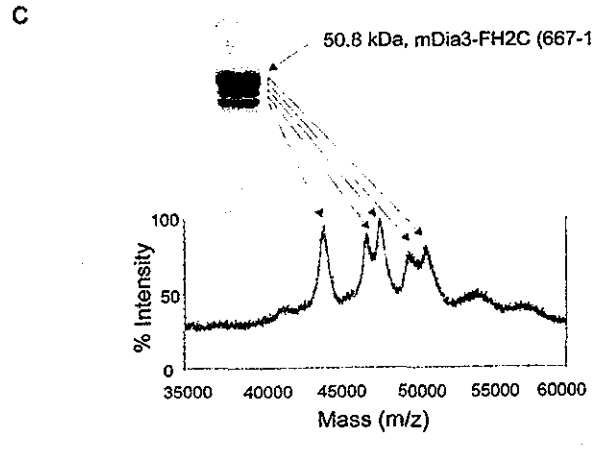
C
50.8 kDa, mDia3-FH2C (667-1102)
% Intensity
100
50
0
35000
40000
45000
50000
55000
60000
Mass (m/z)

necessary for the core FH2 domain to form oligomers and to induce actin polymerization. The structure of the FH2 domain of mouse mDia1 was determined at a resolution of 2.6 Å. The structure exhibited an exclusively helical fold distinct from other known F-actin binding folds and provided implications for the mechanism of formin-mediated actin polymerization.

Results

Identification of a Stable mDia FH2 Core Domain

Initial trials of expression of two FH2 domain constructs from mouse mDia3 (mDia3-FH2N [residues 629–1037] and mDia3-FH2C [residues 667–1102]) were unsuccessful due to their insolubility. Although mDia3-FH2C was partly expressed as a soluble protein and copurified with chaperone, it was unstable and produced several degradation products after purification on a GSH-column (Figure 1C). The mDia3-FH2C was further degraded at 37°C for 5 days to produce a stable 40 kDa fragment (Figure 1; residues 701–1038). Proteolytic digestion of mDia3-FH2C by trypsin and α-chymotrypsin produced fragments of similar or slightly smaller size, indicating that the 40 kDa fragment delineates the FH2 domain. The domain boundaries of the stable fragment were deduced from mass analyses. The corresponding 40 kDa fragments (338 amino acids) from mDia1 or mDia3, and a fragment having in addition to the mDia3-FH2 the linker region between the FH1 and the core FH2 (residues 629–1038) could be stably expressed in large amounts as *E. coli* recombinant proteins.

The Interaction of the Core FH2 Domain with Actin

In preliminary experiments, where the actin was polymerized with 100 mM KCl and 2 mM $MgCl_2$, the effect of 10 μM FH2 was very weak (<5%) due to the relatively high ionic strength (data not shown). To increase the affinity of formin for actin, we used low salt conditions in the assays (see Experimental Procedures). The presence of micromolar concentrations of the core mDia1-FH2 or mDia3-FH2 domains decreased the rate of spontaneous actin polymerization (3.5 μM, 5% pyrene-labeled; Figure 2A). The elongation rates were estimated from the slopes of the normalized pyrene transients at 50% completion of the reaction (insert in Figure 2A). Hyperbola fits to the [FH2] dependence of the elongation rate showed that at saturating [mDia1-FH2] or [mDia3-FH2] the elongation rate decreased to 41 ± 3% or to 26 ± 2% of the value measured in the absence of FH2. Half saturation concentrations were 1.96 ± 0.43 μM and 2.05 ± 0.22 μM, respectively.

The depolymerization rates of actin filaments were measured by diluting actin filaments (5 μM, 68% pyrene-labeled) to 0.1 μM into polymerization buffer alone, or supplemented with mDia1-FH2 or mDia3-FH2. The actin monomer dissociation rates were estimated from the initial slopes of the pyrene transients (first 50 s, Figure 2B) as described in Li and Higgs (2003). The determined rates were plotted as a function of [FH2] and at saturation hyperbolae fits gave 44 ± 6% and 1 ± 4% of the rates measured in the absence of FH2 for mDia1-FH2 and mDia3-FH2, respectively (insert in Figure 2B). Half saturation concentrations were 1.89 ± 0.76 μM and 1.31 ± 0.26 μM, respectively. The effect of mDia1-FH2 on the depolymerization rate of actin filaments (Figure 2B) was similar to the observation that mDia1(549–1255) (involving the FH1 and FH2 domains) decreased the depolymerization rate of actin to ~50% (Li and Higgs, 2003). The difference between the two sets of results is that the effect of mDia1(549–1255) saturated below 50 nM, while mDia1-FH2 in this study saturated at about 2 μM suggesting that the affinity of mDia1-FH2 is much weaker for actin than that of mDia1(549–1255).

The critical concentration of actin was measured in the presence and absence of a series of mDia1-FH2 or mDia3-FH2 concentrations (see Experimental Procedures). The fit to the linear part of the measured fluorescence intensity versus [actin] curves showed that either FH2 fragment increased the critical concentration (Figure 2C). mDia3-FH2 increased the critical concentration of actin from 0.23 μM to ~1 μM (insert in Figure 2C) while the effect of mDia1-FH2 was smaller, increasing the critical concentration to 0.4 μM (insert in Figure 2C). The mDia1-FH2 fragment decreased the elongation rate to ~41% (Figure 2A) and the depolymerization rate to ~44% (Figure 2B), which is consistent with the small mDia1-FH2-induced change of the critical concentration (Figure 2C). In the case of mDia3-FH2 the effect on the dissociation rate was stronger (decreased to <5%) (Figure 2B) while the elongation rate decreased to 26% (Figure 2A), suggesting a decrease in the critical concentration. In contrast with expectation, the critical concentration increased in the presence of mDia3-FH2 (Figure 2C), suggesting that more detailed experimental analysis is required to clarify this discrepancy.

Figure 1. Domain Organization and Primary and Secondary Structure Alignment of the Core FH2 Domain from mDia1

(A) The middle part shows locations of GTPase binding domain (GBD), formin homology domains 1 (FH1), 2 (FH2), and 3 (FH3), linker, and diaphanous autoregulatory domain (DAD) of mDia1. Numbers denote residue number. Fragments used in previous biochemical studies and their location and size relative to mDia1 are indicated above. Fragments of mDia1 and mDia3 used in the present study and their respective length are shown below.

(B) The amino acid sequence of the core FH2 domain of mDia1 (mouse) is compared with those of mDia3 (mouse), Diaphanous (*Drosophila*), Bni1p (*S. cerevisiae*), Cdc12p (*S. pombe*), and FHOD1 (human). Amino acid residues conserved in all the six aligned formin family proteins are colored orange, whereas those conserved in five out of six proteins are colored yellow. An open box indicates the location of the highly conserved G-N-X-M-N motif. Arrowheads indicate positions of mutated residues Ile845 and Met970. Filled circles indicate positions of three Lys residues whose replacement with Ala abolished alignment of microtubules and bundling of F-actin (see text). Open circles indicate residues replaced in Bni1p temperature-sensitive mutants (see text). Secondary structure elements of the FH2 domain obtained from the structure determination are indicated below the amino acid sequence. Regions corresponding to the NH_2-terminal, three-helix-bundle, and the FH2 motif subdomains are colored red, blue, and green, respectively.

(C) SDS gel showing the degradation of the mDia3 FH2C (top) and the corresponding mass spectrometric analysis (bottom). Masses were obtained from MALDI-TOF-MS.

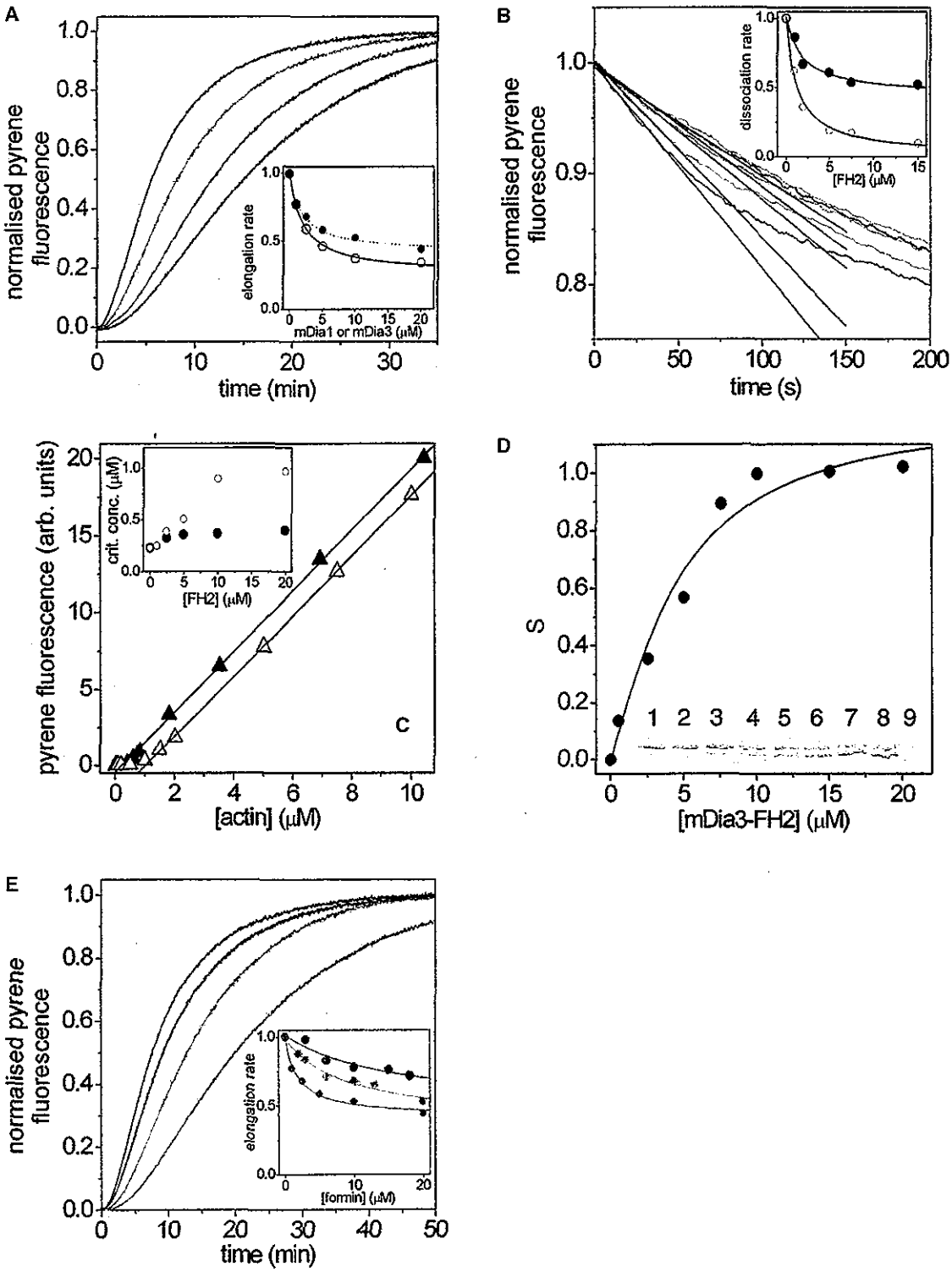

Figure 2. Biochemical Analysis of the Core FH2 Domain

(A) Polymerization. Actin monomers (3.5 μM, 5% pyrene-labeled) were polymerized in the absence or presence of FH2 fragments, and the pyrene fluorescence was monitored. The figure shows the normalized pyrene fluorescence transients obtained at different [mDia1-FH2] (0 μM [black], 2.5 μM [red], 5 μM [green], and 10 μM [blue]). Similar experiments were carried out with mDia3-FH2 as well (traces are not shown). The insert shows the relative elongation rate (estimated from the slopes at 50% saturation) as a function of [mDia1-FH2] (filled circles) or of [mDia3-FH2] (empty circles). Hyperbola fits to the mDia1-FH2 (dashed line) data and to the mDia3-FH2 (solid line) data are superimposed.

(B) Depolymerization. Actin (5 μM, 68% pyrene-labeled) was polymerized and diluted to 0.1 μM into polymerization buffer alone or to polymerization buffer supplemented with FH2. The figure shows the normalized fluorescence transients measured at different [mDia1-FH2] (0 μM [black], 1 μM [red], 2 μM [green], 5 μM [blue], and 7 μM [magenta]). Linear fits to the first 50 s are shown as solid lines. Similar experiments were carried out with mDia3-FH2 as well (traces are not shown). The insert shows the relative dissociation rate (slope of the

It was shown that the mDia1(549–1255) fragment involving the FH1, linker, FH2, DAD, and C terminus can bind to preformed actin filaments (Li and Higgs, 2003). To test whether our FH2 fragments retain this ability, we estimated the affinity of FH2 for actin filaments in cosedimentation assays (see Experimental Procedures). Polyacrylamide gel analysis shows (Figure 2D) that mDia3-FH2 (lower band) is cosedimented with preformed actin filaments (upper band) in a 1:1 complex with actin protomer. Due to the fraction of actin below the critical concentration, some actin remained in the supernatant, the amount of which increased by a factor of ~3 at [mDia3-FH2] >10 μM relative to that in the absence of mDia3 FH2 (insert in Figure 2D), consistent with mDia3-FH2-induced increase of the critical concentration (Figure 2C). Lane 9 shows that excess mDia3-FH2 in the absence of actin does not precipitate. The analysis of the gels (Equation 1) gave a K_D of 2.9 ± 1.2 μM for mDia3-FH2 binding to F-actin (Figure 2D). mDia1-FH2 also bound to actin filaments but the S versus [mDia1-FH2] plot (see Experimental Procedures) did not saturate below 20 μM mDia1-FH2 (data not shown), suggesting that the binding was weaker.

The mDia1(549–1255) fragment bound preformed actin filaments with an apparent K_D of 3 μM (Li and Higgs, 2003). Our result with mDia3-FH2 (2.9 ± 1.2 μM, Figure 2D) was close to the value obtained with mDia1(549–1255). Although we used lower salt conditions, the affinity of mDia1-FH2 in our experiments was weaker than that of mDia1(549–1255) (Li and Higgs, 2003), indicating that regions outside the FH2 domain contribute to the binding of mDia1 to preformed actin filaments. The half saturation of the effects of both mDia1-FH2 and mDia3-FH2 on the elongation or depolymerization was between 1 and 2 μM (Figures 2A and 2B). The affinity of mDia3-FH2 for actin filaments is close to this concentration range, but the affinity of mDia1-FH2 for actin is much weaker. For mDia1(549–1255) the K_D for the affinity to actin filaments was 3 μM, while the effect of mDia1(549–1255) on the kinetics parameters was in the nanomolar range. All these points to the conclusion, that there is no obvious correlation between the affinity of the formin fragments for preformed actin filaments and their effect on the polymerization of actin.

Overall Structure of the Core FH2 Domain of mDia1

The crystal structure of the mDia1-FH2 (338 amino acid residues, 40 kDa) was determined at 2.6 Å resolution (Table 1). The asymmetric unit of the crystal contained four molecules, denoted A, B, C, and D (Figure 3A). The present model contains residues 829–960 and 985–1160 of molecule A, residues 830–1150 of molecule B, residues 829–952, 955–962, and 1000–1150 of molecule C, and residues 830–963 and 985–1150 of molecule D. The other parts of the molecules had poor or uninterpretable electron densities and could not be modeled. The missing residues are located either at the N terminus, C terminus, or in a region covering the conserved FH2 motif of approximately 70 residues (see below). The electron densities for the region covering the FH2 motif were best defined for the molecule B probably due to crystal packing, and a representative example of the map is shown in Figure 3B. Since the visible parts are very similar in the four molecules, besides some hinge-bending movement of molecules A/C compared to B/D (see below), we will hereafter describe the structure of the FH2 domain based on molecule B unless mentioned otherwise.

The FH2 domain is an elongated crescent-shaped molecule with an approximate size of 100 Å by 25 Å by 25 Å composed exclusively of α helices (Figure 4A). The structure of the FH2 domain can be divided into three subdomains: the NH_2-terminal subdomain (red), the three-helix-bundle subdomain (blue), and the FH2 motif (green) because the latter encompasses the region originally defined and still documented as FH2 (Castrillon and Wasserman, 1994; Watanabe et al., 1997; Wallar and Alberts, 2003).

The Subdomains

The NH_2-terminal subdomain (84 aa) is composed of five α helices. DALI search (Holm and Sander, 1994) found six proteins as structural homologs. However, the Z scores between the NH_2-terminal subdomain and those proteins are low (Z < 2.4). From the low similarity, it seems unlikely that there are any functional or evolutionary connections between them.

The three-helix-bundle subdomain is composed of three antiparallel α helices, which form a left-handed coiled-coil structure. DALI search found a number of structural homologs, such as syntaxin1a (Z = 9.5, PDB code 1br0) (Fernandez et al., 1998), Smac/DIABLO (Z = 8.6, PDB code 1few) (Chai et al., 2000), spectrin-repeats of spectrin (Z = 8.6, PDB code 1cun) (Grum et al., 1999), and α-actinin (Z = 8.0, PDB code 1quu) (Djinovic-Carugo et al., 1999). Most of these proteins have three- or four-

linear fits) as a function of [mDia1-FH2] (filled circles) or [mDia3-FH2] (empty circles). Hyperbola fits to the data are shown as solid lines.

(C) Effect on the critical concentration of actin assembly. Actin (5% pyrene-labeled) was incubated overnight at different concentration in polymerization buffer alone or in the presence of mDia1-FH2 or mDia3-FH2. The formin concentrations were 0, 1, 2.5, 5, 10, and 20 μM. The figure shows the [actin] dependence of the pyrene fluorescence intensities measured in the absence of formin (filled triangles) or in the presence of 20 μM mDia3-FH2 (empty triangles). Fits to the linear part of the intensity versus [actin] curves gave critical concentrations of 230 nM in the absence of formin. The insert shows the [mDia1-FH2] (filled circles) or [mDia3-FH2] (empty circles) dependence of the critical concentration.

(D) Affinity for F-actin. Fraction of mDia3-FH2 bound to F-actin (S) calculated from the results of SDS-PAGE analysis of a cosedimentation assay. The analysis with Equation 1 (solid line, see Experimental Procedures) gave an apparent K_D = 2.9 ± 1.2 μM. The insert shows the gel (12.5%) of the pellet, obtained with [actin] = 3 μM and [mDia3-FH2] of 0, 0.5, 2.5, 5, 7.5, 10, 15, and 20 μM (lanes 1–8). Lane 9 is obtained with 5 μM mDia3 FH2 in the absence of actin.

(E) Mutational analysis. Normalized pyrene fluorescence transients obtained when 3.5 μM actin (5% pyrene-labeled) was polymerized in the absence of formin (black) or in the presence of 10 μM I845R (blue), 10 μM M970R (red), or 10 μM wild-type mDia1-FH2 (green). The insert shows the formin dependence of the relative elongation rates (estimated from the slopes at 50% saturation) for I845R (blue circles), M970R (red circles), and wild-type mDia1-FH2 (green). The mDia1-FH2 data are taken from (A); hyperbola fits are superimposed as solid lines.

Table 1. Data Collection, Phasing, and Refinement Statistics

	Native	SeMet
Diffraction Data		
Temperature (K)	100	100
Space group	$P2_12_12_1$	$P2_12_12_1$
Unit-cell parameters (Å)		
a	82.43	82.47
b	124.52	119.78
c	229.40	246.41
Wavelength (Å)	0.9340	0.9786
Resolution (Å)	50.0–2.6	50.0–3.4
Unique reflections	73,264	34,362
Total reflections	406,569	491,435
I/σ	18.8 (5.4)	28.4 (9.4)
R_{merge}[a]	9.9 (49.5)	10.2 (49.0)
Completeness (%)	99.6 (99.9)	99.7 (100.0)
Phasing Statistics		
Number of sites		52
Phasing power		
Anomalous (acentrics)		2.516
R_{cullis}[b]		
Anomalous (acentrics)		0.6125
Mean overall figure of merit		
Acentric		0.5248
Centric		0.2569
Refinement Statistics		
Protein atoms	9876	
Water oxygens	191	
Sulfate Ions	3	
R_{work}[c] (%)	22.99	
R_{free}[d] (%)	26.68	
Rms deviation from ideal values		
Bond length, Å	0.0064	
Bond angles, degrees	1.12	
Improper angles, degrees	0.74	
Average B factor, Å^2		
Molecule A	64.0	
Molecule B	52.8	
Molecule C	79.2	
Molecule D	90.0	
Solvent	59.4	
Sulfates	51.1	

Values in parentheses are for the highest resolution shell.
[a] $R_{merge} = \Sigma_h \Sigma_i |I_{hi} - \langle I_h \rangle| / \Sigma_h \Sigma_i |I_{hi}|$, where h refers to unique reflection indices and i indicates symmetry-equivalent indices.
[b] $R_{cullis} = \Sigma[|F_H| - (|F_{PH}| - |F_P|)] / \Sigma(|F_{PH}| - |F_P|)$, where $|F_H|$ represents the calculated heavy-atom structure factor.
[c] $R_{work} = \Sigma||F_O| - |F_C|| / \Sigma|F_O|$ for the working set reflections (90% of the data) used for the refinement.
[d] $R_{free} = \Sigma||F_O| - |F_C|| / \Sigma|F_O|$ for the test set reflections (10% of the data) excluded from the refinement.

helix-bundle structures. The resemblance of the FH2 domain to spectrin-repeats is particularly intriguing because spectrin-repeat-containing proteins such as spectrin and α-actinin also bind to F-actin (Grum et al., 1999; Djinovic-Carugo et al., 1999). The three-helix-bundle subdomain of FH2 and one unit of spectrin-repeats are similar in size (approximately 100 aa) and also in geometry, which is shown by an rms deviation between corresponding Cα atoms of 2.3 Å over 69 residues.

The three α helices form an extensive hydrophobic core. There is, however, a buried salt bridge between Arg919 in α6 and Asp1067 in a loop region between helices α11 and α12 (Figure 4B). These two residues are highly conserved and most likely contribute to the conformation of the loop region. In Bni1p, both Arg1528 and Arg1530 were found mutated to Ala in a temperature-sensitive mutant (Sagot et al., 2002a). Arg1528 corresponds to Arg919 of mDia1. Since replacement of Arg1528 by Ala disrupts the salt bridge, the mutation most probably destabilizes the three-helix-bundle structure and/or the interface between the three-helix-bundle and the NH_2-terminal subdomains. On the other hand, additional replacement of Arg1530 by Ala seems less important for the temperature sensitivity of Bni1p because the side chain of the corresponding Asn921 of mDia1 is exposed to solvent and seems to have no important interactions with other residues.

The FH2 motif is composed of two nonconsecutive parts of the polypeptide chains. The first segment (residues 953–1026) is located between α6 and α11 of the three-helix-bundle subdomain. It includes residues (946–1010) originally identified as FH2 (Watanabe et al., 1999) and is the evolutionary best-conserved region of the formin-family proteins (Figure 1B). The highly conserved ^{967}GNXMN^{971} motif is located at the COOH-terminal end of α7 (Figure 4A). The region around this motif is apparently very flexible, since it is only partially visible in molecules A, C, and D of the asymmetric unit. The invariant Gly967, Asn968, and highly conserved (in five of six, see Figure 1) Met970 and Asn971 seem to play structural roles where Gly967 has ϕ,ψ angles (−87, −17) not allowed for any other residue and appears to induce a particular angle of the polypeptide chain at the end of α7. Lys989, Lys994, and Lys999 are located at a tip of the FH2 motif where many conserved residues cluster (Figure 4D).

Replacement of these Lys residues by Ala abolished the alignment of microtubules and the bundling of F-actin induced by an activated mutant of mDia1 in vivo (Ishizaki et al., 2001). These Lys residues together with surrounding conserved residues may constitute the binding interface with other proteins such as F-actin. The second segment of the subdomain is formed by the long α helix (α13) and a short connecting linker. α13 sits in a cleft formed by α8, α9, a 3_{10} helix (3_{10}), α10, and connecting loops of the first segment of the subdomain.

Superimposing molecules A, C, and D on the three-helix-bundle subdomains, only the FH2 motif shows significant differences in structure between molecules B/D and A/C (Figure 4C), suggesting conformational flexibility of this region. Although only helices α9 and α13 are clearly defined in all four molecules, it appears that the FH2 motif shifts as a rigid body such that the helix α13 moves by an angle of 20°–25° relative to the three-helix-bundle subdomain (Figure 4C). It would be attractive to assume that these observed differences in structure are indicative of a conformational change that is relevant to the function of mDia1. In favor of this we note that the C-terminal helix α13 is directly linked to the autoinhibitory DAD domain whose importance for mDia regulation has been well documented (Watanabe et al., 1999; Alberts, 2001).

It was reported that an mDia1-FH2 construct encompassing residues 736–1150 induces SRF activation in vivo, which is mediated by its actin polymerization activity (Copeland and Treisman, 2002). However, C-terminal deletion of residues 1130–1150 abolished the activity of the construct for SRF activation (Copeland and Treis-

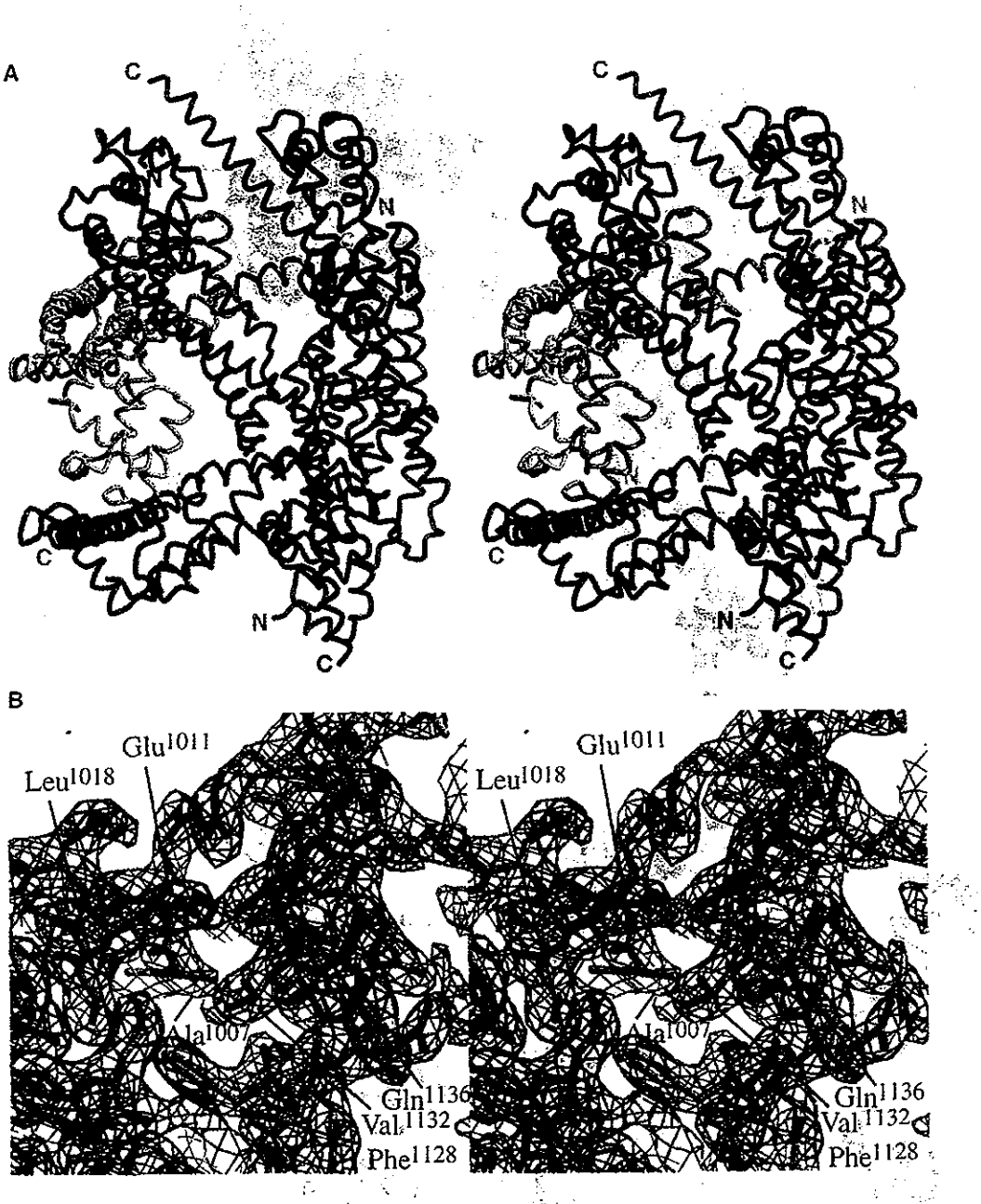

Figure 3. X-Ray Structure Solution of the Core FH2 Domain from mDia1

(A) Stereo view of the asymmetric unit. Molecules A, B, C, and D of the asymmetric unit are colored red, green, blue, and yellow, respectively, with NH_2 and COOH termini labeled correspondingly.

(B) A representative stereo electron density map. An $2F_o - F_c$ electron density map, contoured at 1.2σ, of the interface between α13 and surrounding helices α9 and 3^{10}. The residues involved in the interaction are labeled.

man, 2002). From the present structure, it is clear that the deletion of residues 1130–1150 severely disturbs the integrity of the FH2 motif since these residues are involved in a number of interactions. Thus, extensive hydrogen-bonding networks are formed between Glu1134 and His1004, Gln1136 and Glu1011, Arg1138 and Glu1008, and Arg1139 and Glu1011 (Figure 3B). Moreover, Val1132 is involved in a hydrophobic core together with Ala1007, Leu1018, and Phe1128 (Figure 3B).

Both Ends of FH2 Are Required for Activity

In order to find out whether both ends of the elongated FH2 protein are required for the inhibition of actin polymerization, we used the structure to design mutants of exposed residues in the most highly conserved regions of the protein surface, as indicated in Figure 4D. When 30 different formin sequences were aligned and the conserved residues were mapped on the surface of the molecule, clustering of conserved residues around Met970 and Ile845 were prominent (only six sequences are shown, Figure 1B). Since hydrophobic residues are rarely exposed to the solvent, we suspected that one or both of these residues are involved in interaction with actin. Therefore, we replaced these hydrophobic residues with the more hydrophilic arginine.

The mutants M970R and I845R were soluble, stable, and could be purified as for the wild-type protein. To investigate the effect of the mutations, the spontaneous